Probing the role of synaptic adhesion molecule RTN4RL2 in setting up cochlear connectivity

Nare Karagulyan[1,2,3#], Maja Überegger[4#], Yumeng Qi[5#], Norbert Babai[1,2], Florian Hofer[4], Lejo Johnson Chacko[6], Fangfang Wang[5], Maria Luque[6], Rudolf Glueckert[6], Anneliese Schrott-Fischer[6], Yunfeng Hua[5*], Tobias Moser[1,2,3,7*], Christine Bandtlow[4*]

[1]Institute for Auditory Neuroscience, University Medical Center Göttingen, Göttingen, Germany

[2]Auditory Neuroscience and Synaptic Nanophysiology Group, Max Planck Institute for Multidisciplinary Sciences, Göttingen, Germany

[3]Cluster of Excellence "Multiscale Bioimaging of Excitable Cells", 37075 Göttingen, Germany

[4]Institute of Neurobiochemistry, Biocenter, Medical University of Innsbruck, 6020 Innsbruck, Austria

[5]Shanghai Institute of Precision Medicine, Ninth People's Hospital, Shanghai Jiao Tong University School of Medicine, 200125 Shanghai, China

[6]Department of Otorhinolaryngology, Medical University of Innsbruck, 6020 Innsbruck, Austria

[7]Department for Hearing, Speech and Voice Disorders, Medical University of Innsbruck, 6020 Innsbruck, Austria

Running title: Expression and function of RTN4RL2 in the cochlea

[#]equal contribution
*correspondence to
Dr. Christine Bandtlow: christine.bandtlow@i-med.ac.at
Dr. Tobias Moser: tmoser@gwdg.de
Dr. Yunfeng Hua: yunfeng.hua@shsmu.edu.cn

Abstract

Sound encoding depends on the precise and reliable neurotransmission at the afferent synapses between the sensory inner hair cells (IHCs) and spiral ganglion neurons (SGNs). The molecular mechanisms contributing to the formation, as well as interplay between the pre- and postsynaptic components remain largely unclear. Here, we tested the role of the synaptic adhesion molecule and Nogo/RTN4 receptor homolog RTN4RL2 (also referred to as NgR2) in the development and function of afferent IHC-SGN synapses. Upon deletion of RTN4RL2 in mice (RTN4RL2$^{-/-}$), presynaptic IHC active zones showed enlarged synaptic ribbons and a depolarized shift in the activation of $Ca_V1.3$ Ca^{2+} channels. The postsynaptic densities (PSDs) of SGNs were smaller and deficient of GluA2-4 AMPA receptor subunits despite maintained Gria2 mRNA expression in SGNs. Next to synaptically engaged PSDs we observed "orphan" PSDs located away from IHCs. They likely belong to a subset of SGN peripheral neurites that

do not contact the IHCs in RTN4RL2$^{-/-}$ cochleae as found by volume electron microscopy reconstruction of SGN neurites. Auditory brainstem responses of RTN4RL2$^{-/-}$ mice showed increased sound thresholds indicating impaired hearing. Together, these findings suggest that RTN4RL2 contributes to the proper formation and function of auditory afferent synapses and is critical for normal hearing.

Introduction

Hearing relies upon the correct formation and maturation of cochlear afferent synapses between postsynaptic type I spiral ganglion neurons (SGNs) and presynaptic inner hair cells (IHCs; reviewed in Johnson et al., 2019; Bulankina and Moser, 2012; Appler and Goodrich, 2011). In mice, SGN neurites extend and reach IHCs at late embryonic stages (E16.5; Koundakjian, Appler, and Goodrich, 2007), whereby early synaptic contacts are established between the two cells at E18 (Michanski et al., 2019). Developmental changes and maturation of afferent synapses continue until the onset of hearing (p12), with further refinement occurring till the fourth postnatal week (Wong et al., 2014; Liberman and Liberman, 2016; Michanski et al., 2019). In mature cochleae, each IHC receives a contact from 5-30 SGNs, while each SGN contacts only one active zone (AZ) of one IHC in the majority of cases (Meyer and Moser, 2010; Hua et al., 2021).

To this date, multiple mechanisms have been implicated in SGN neurite guidance and establishment of IHC innervation by SGNs, including signaling via EphrinA5-EphA4, Neuropilin2/Semaphorin3F, Semaphorin5B/PlexinA1, Semaphorin3A (Defourny et al., 2013; Coate et al., 2015; Jung et al., 2019; Cantu-Guerra et al., 2023). Less is known about the molecules governing the transsynaptic organization at IHC afferent synapses. Similar to the central conventional synapses, synaptic adhesion proteins such as neurexins and neuroligins have been suggested to play a role in pre- and postsynaptic assemblies (Ramirez et al., 2022; Jukic et al., 2024). Furthermore, the $Ca_V1.3$ extracellular auxiliary subunit $Ca_V\alpha_2\delta_2$ was indicated to be important for proper alignment of presynaptic IHC AZs and postsynaptic densities (PSDs) of SGNs (Fell et al., 2015).

Whether reticulon 4 receptors (RTN4Rs) contribute to setting up afferent connectivity in the cochlea remained to be investigated. The RTN4 receptor family consists of 3 homologous proteins RTN4R, RTN4RL1 and RTN4RL2. RTN4Rs are leucine-rich repeat (LRR)

63 and glycosylphosphatidylinositol (GPI) anchored cell surface receptors (Figure 1A). Their
64 primary role is thought to limit synaptic plasticity and axonal outgrowth as well as to restrict
65 axonal regeneration after injury (reviewed in Mironova and Giger, 2013). While RTN4R and
66 RTN4RL1 are involved in axonal guidance (Vaccaro et al., 2022), RTN4RL2 has been proposed
67 to be important for innervation of the epidermis by dorsal root ganglion neurons (Bäumer et
68 al., 2014). Furthermore, RTN4Rs are suggested to control the number and the development
69 of synapses (Wills et al., 2012) and to play a role in transsynaptic signaling (Wang et al., 2021).
70 Recent single-cell transcriptomic studies of the cochlea detected the expression of
71 RTN4Rs in SGNs and IHCs (Shrestha et al., 2018; Jean et al., 2023). Here, we investigated the
72 role of RTN4RL2 in the cochlea using previously described RTN4RL2 constitutive knock-out
73 mice (RTN4RL2$^{-/-}$; (Wörter et al., 2009)). We found RTN4RL2 to be expressed in SGNs and to
74 be required for normal hearing: auditory brainstem responses were impaired upon RTN4RL2
75 deletion. We discovered both pre- and postsynaptic alterations of IHC-SGN synapses in
76 RTN4RL2$^{-/-}$ mice: presynaptic Ca^{2+} channels of IHCs required stronger depolarization to
77 activate and PSDs seemed deficient of GluA2-4 AMPA receptor subunits. Additionally, a subset
78 of type I SGN neurites did not contact IHCs but likely still feature “orphan” PSDs.

79 Results

80 RTN4RL2 is expressed both in hair cells and spiral ganglion neurons

81

82 Recent transcriptomic data had detected RTN4RL2 expression both in hair cells and SGNs
83 (Elkon et al., 2015; Liu et al., 2018; Shrestha et al., 2018; Jean et al., 2023). We verified this by
84 performing RNAscope staining in cochleae during inner ear development. We observed
85 RTN4RL2 mRNA expression at E11.5 in the hair cell region and at E12.5 in both the spiral
86 ganglion and hair cells (Figure 1B, C). RTN4RL2 expression was further evident in hair cells at
87 E16.5 and p1 (Figure 1D, E) and was maintained at low levels in spiral ganglia of p40 mice
88 (Figure 1F). RTN4RL2$^{-/-}$ mice were lacking RTN4RL2-specific mRNA puncta (Figure 1F),
89 demonstrating specific detection of RTN4RL2 expression in SGNs.

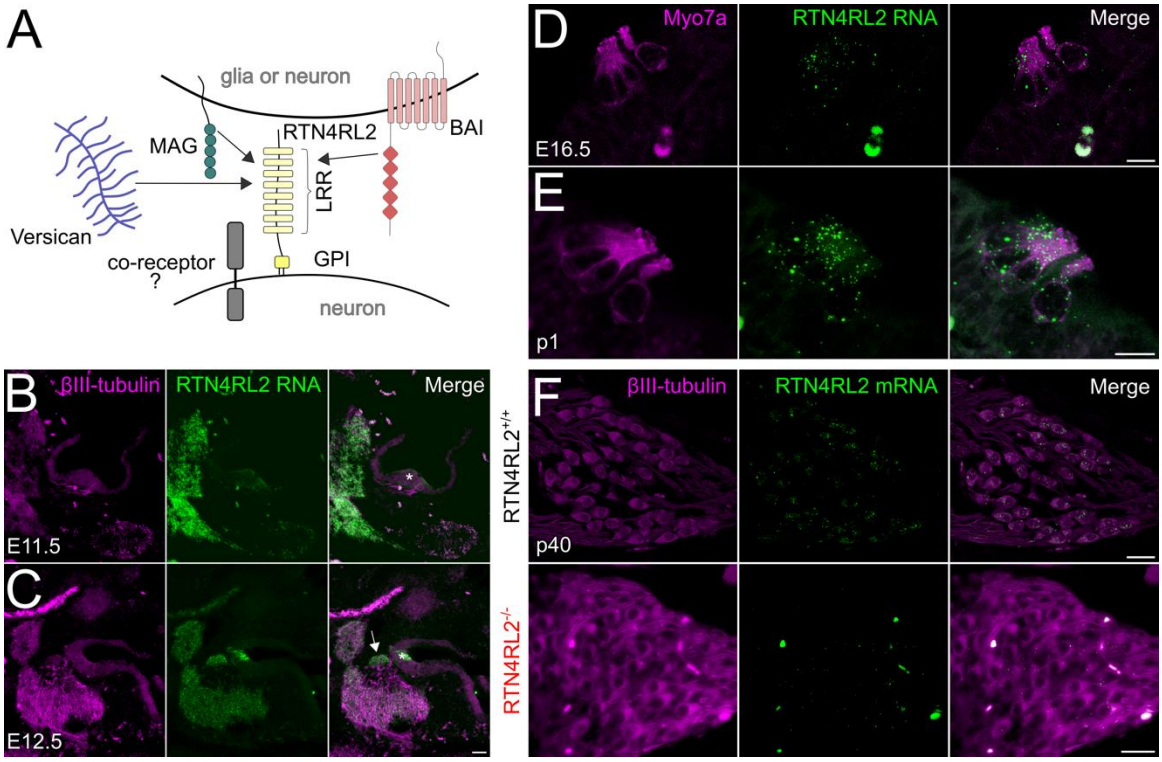

Figure 1. RTN4RL2 mRNA expression in IHCs and SGNs of the mouse cochlea. (**A**) RTN4RL2 is an LRR protein and is anchored to the cell membrane via GPI. In the nervous system RTN4RL2 has been implicated to interact with MAG, versican, BAI (Venkatesh et al., 2005; Bäumer et al., 2014; Wang et al., 2021). (**B, C**) Exemplary images of RNAscope ISH for RTN4RL2 mRNA (green) in the otic vesicles of E11.5 (B) and E12.5 (C) mice. Scale bar = 50 µm. The developing organ of Corti region is marked with an asterisk and the spiral ganglion is indicated with an arrow. (**D, E**) Exemplary images of RTN4RL2 RNA expression in hair cells of E16.5 (D) and p1 (E) mice. Hair cells are visualized with anti-Myo7a stainings. Scale bars = 10 µm. (**F**) Representative images of RNAscope ISH for RTN4RL2 mRNA (green dots) combined with immunostaining for neuron-specific marker βIII-tubulin (grey) in paraffin sections of p40 RTN4RL2$^{+/+}$ and RTN4RL2$^{-/-}$ cochleae. Scale bars = 20 µm.

RTN4RL2 is important for the correct development of the auditory afferent synapses

To probe the role of RTN4RL2 in the cochlea, we first studied the numbers of cochlear cells in RTN4RL2$^{-/-}$ mice. We did not observe any change in SGN density or counts of inner and outer hair cells at p15, 1-month- and 2-month-old mice (Figure 2-figure supplement 1). Given that RTN4RL2 has been implicated in synapse formation and development (Wills et al., 2012; Borrie et al., 2014; Wang et al., 2021) we immunolabeled IHC afferent synapses for presynaptic RIBEYE/Ctbp2 and postsynaptic Homer1 in mice at the age of 3 weeks. While we did not detect any change in the number of synaptic ribbons in RTN4RL2$^{-/-}$ IHCs, ribbon volumes were bigger

112 (Figure 2C, D; Figure 2-figure supplement 2). Interestingly, in addition to the Homer1 positive
113 puncta juxtaposing presynaptic ribbons, we observed additional Homer1 patches, which
114 appeared to be away from IHCs, potentially marking “orphan” PSDs (Figure 2A, B). Moreover,
115 the Homer1 puncta juxtaposing IHC AZs were significantly smaller in RTN4RL2$^{-/-}$ mice
116 compared to the control IHCs (Figure 2E). While we found the percentage of presynaptic
117 ribbons juxtaposing Homer1 immunofluorescent puncta to be decreased by approximately
118 7% in RTN4RL2$^{-/-}$ mice (Figure 2F), we cannot exclude that our immunolabeling protocol lacked
119 the sensitivity to detect smaller synaptically engaged PSDs. Out of the four pore-forming
120 AMPA receptor subunits (GluA1-4), mature SGNs express GluA2-4 (Niedzielski and Wenthold,
121 1995; Matsubara et al., 1996). Our immunolabeling of anti-GluA2/3 revealed a severe
122 reduction in the number of GluA2/3 positive puncta in RTN4RL2$^{-/-}$, indicating possible lack or
123 decrease of GluA2/3 (Figure 3A, B). Interestingly, the remaining GluA2/3 patches did not
124 properly juxtapose presynaptic ribbons (Figure 3C). Despite this, the expression of Gria2
125 mRNA appeared to be maintained in SGNs, as indicated by RNAscope (Figure 3D). We then
126 checked whether the potential lack of GluA2/3 was accompanied by an increase in GluA4
127 signal at the PSDs of RTN4RL2$^{-/-}$ SGNs, as was previously shown in GluA3 KO mice (Rutherford
128 et al., 2023). Surprisingly, we did not detect a significant GluA4 signal compared to the
129 background in RTN4RL2$^{-/-}$ cochleae (Figure 3-figure supplement 1). To check if the “orphan”
130 PSDs away from IHCs were possibly erroneously engaged with efferent presynaptic terminals
131 we stained the latter for synapsin, which is lacking from IHCs, but did not observe any obvious
132 juxtaposition between the “orphan” Homer1 and synapsin puncta (Figure 2-figure
133 supplement 3).

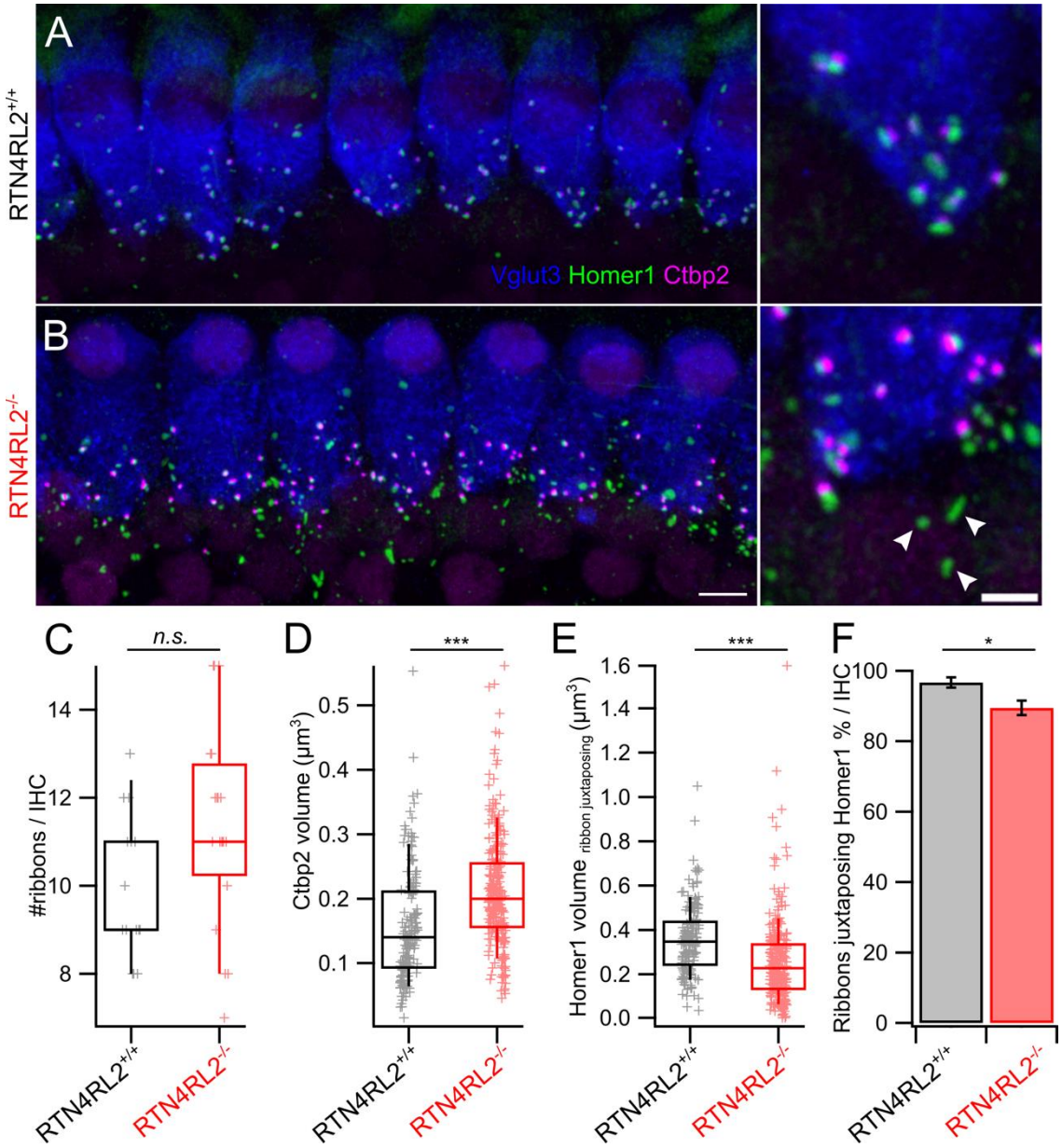

Figure 2. Pre- and postsynaptic changes at IHCs of RTN4RL2$^{-/-}$ mice. (**A, B**) Maximum intensity projections of representative confocal stacks of IHCs from apical cochlear region of 3-week-old RTN4RL2$^{+/+}$ (A) and RTN4RL2$^{-/-}$ (B) mice immunolabeled against Vglut3, Homer1, and Ctbp2. Scale bar = 5 µm. Images on the right-hand side are zoomed into the synaptic regions. Scale bar = 2 µm. Some of the putative "orphan" PSDs are marked with the white arrowheads. (**C**) Number of Ctbp2 positive puncta is not changed in IHCs of RTN4RL2$^{-/-}$ mice (RTN4RL2$^{+/+}$: 9.9 ± 0.42, SD = 1.62, n = 15, N = 2 vs RTN4RL2$^{-/-}$: 11.4 ± 0.5, SD = 2.25, n = 20, N = 3; p = 0.06, Mann-Whitney-Wilcoxon test). (**D**) Ribbon volumes are enlarged in RTN4RL2$^{-/-}$ IHCs (RTN4RL2$^{+/+}$: 0.16 ± 0.007 µm^3, SD = 0.09 µm^3, n = 165, N = 2 vs RTN4RL2$^{-/-}$: 0.21 ± 0.005 µm^3, SD = 0.09 µm^3, n = 259, N = 3; p < 0.001, Mann-Whitney-Wilcoxon test). (**E**) Homer1 patches which are juxtaposing presynaptic ribbons show decreased volumes in RTN4RL2$^{-/-}$ IHCs (RTN4RL2$^{+/+}$: 0.36 ± 0.01 µm^3, SD = 0.16 µm^3, n = 160, N = 2 vs RTN4RL2$^{-/-}$: 0.26 ± 0.01 µm^3, SD = 0.19 µm^3, n = 249, N = 3; p < 0.001, Mann-Whitney-Wilcoxon test). (**F**) Percentage

of Ctbp2 puncta juxtaposing Homer1 is slightly decreased in RTN4RL2$^{-/-}$ mice (RTN4RL2$^{+/+}$: 96.7 ± 1.45 %, SD = 5.44 %, n = 14, N = 2 vs RTN4RL2$^{-/-}$: 89.5 ± 2.05 %, SD = 9.18 %, n = 20, N = 3; p = 0.03, Mann-Whitney-Wilcoxon test). Data is presented as mean ± SEM. Box-whisker plots show the median, 25/75 percentiles (box), and 10/90 percentiles (whiskers). Individual data points are overlaid.

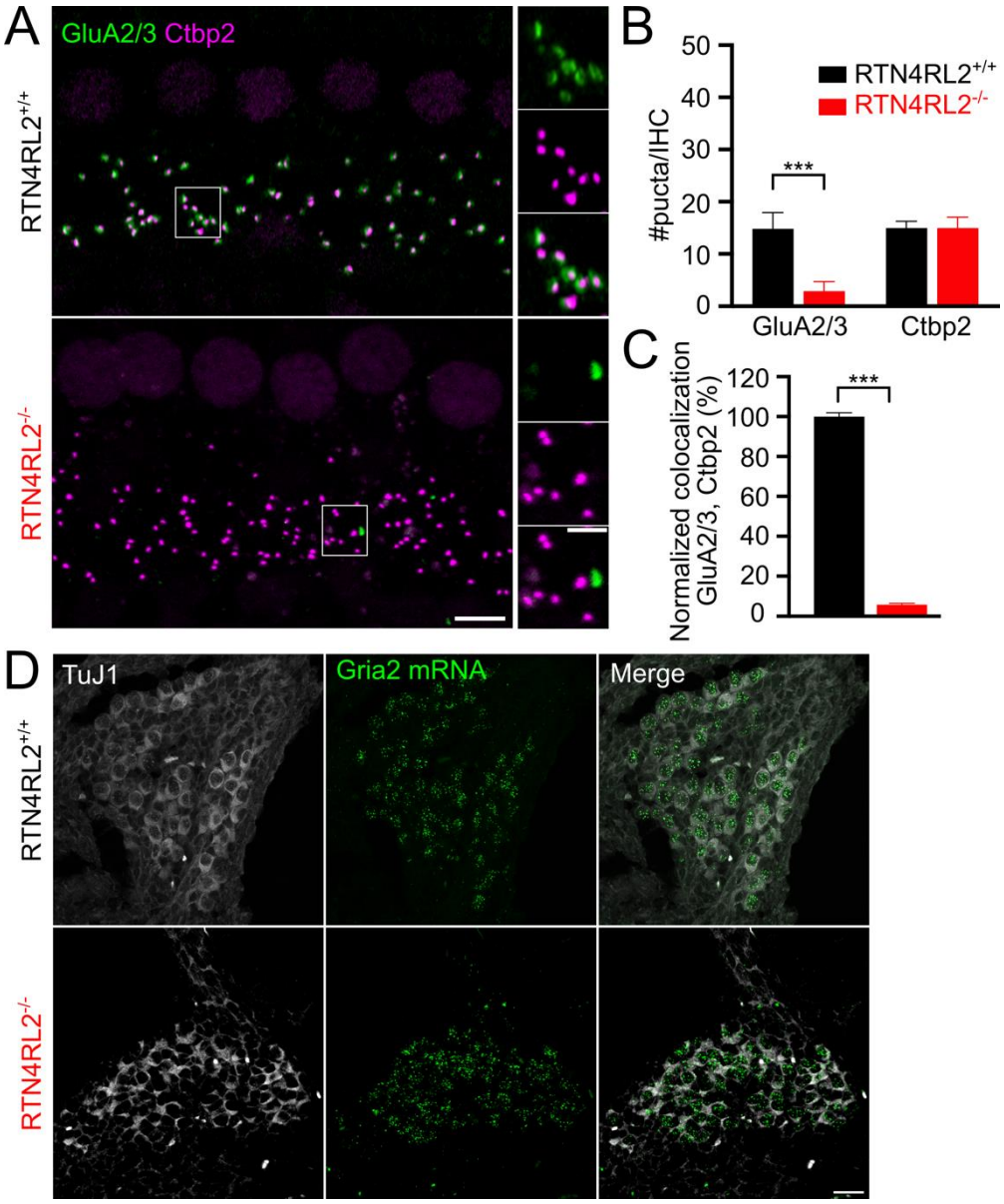

Figure 3. Reduced GluA2/3 signal juxtaposing presynaptic ribbons in IHCs of RTN4RL2$^{-/-}$ mice. (**A**) Maximum intensity projections of representative IHC regions from 1- to 1.5-month-old RTN4RL2$^{+/+}$ (top) and RTN4RL2$^{-/-}$ (bottom) mouse cochleae immunolabeled against Ctbp2/Ribeye (ribbons) and GluA2/3 (AMPA receptors of PSD). Scale bar = 5 µm. The zoom-in regions marked with the white rectagles are presented on the right-hand side. Scale bar = 2 µm. (**B**) The number of the GluA2/3 positive puncta is drastically reduced in RTN4RL2$^{-/-}$ mice despite the maintained number of presynaptic ribbons ($p < 0.001$, Mann-Whitney-Wilcoxon test). (**C**) Disrupted colocalization of Ctbp2/Ribeye and GluA2 immunofluorescence puncta at IHCs of RTN4RL2$^{-/-}$ mice ($p < 0.001$, Mann-Whitney-Wilcoxon test). N = 6 animals/genotype.

164 (**D**) Representative images of RNAscope ISH from p4 mice show maintained expression of
165 Gria2 (red dots) in the SGN somata of RTN4RL2$^{-/-}$ mice. Scale bar = 20 μm.
166

167 ## Additional non-synaptic neurites in the cochlea of RTN4RL2$^{-/-}$ mice

168

169 To further examine the afferent cochlear connectivity, we utilized serial block-face scanning
170 electron microscopy (SBEM) to 3D reconstruct the apical cochlea segments from two
171 RTN4RL2$^{-/-}$ and one littermate RTN4RL2$^{+/+}$ control mice at p36 (Figure 4A). As recently
172 demonstrated (Hua et al., 2021; Lu et al., 2024), the spatial resolution of SBEM allows reliable
173 ribbon synapse identification and neurite reconstruction (Figure 4B and C). In these three
174 datasets, we have traced all neural fibers from the habenula perforata (three in each dataset).
175 This resulted in 133 fibers, of which 115 were classified as peripheral neurites of type I SGN
176 based on their radial calibers and extensive myelination after entering the habenula perforata
177 (Figure 4D). We observed a substantial number of neurites that did not engage the IHCs (non-
178 synaptic neurites) in the RTN4RL2$^{-/-}$ organs of Corti (23 out of 83) in contrast to the wild-type
179 control (3 out of 32, Figure 4E). Although most non-synaptic neurites were found in the inner
180 spiral bundle, they failed to reach IHC basal lateral poles to form contacts (17 out of 23 in
181 RTN4RL2$^{-/-}$ animals). This result might provide a plausible explanation for the "orphan"
182 Homer1 puncta shown by immunohistochemistry in RTN4RL2$^{-/-}$ organs of Corti. Note that the
183 presence of non-synaptic neurites in the RTN4RL2$^{-/-}$ animal was not associated with a
184 profound reduction in ribbon synapses (Figure 2C, Figure 2-figure supplement 2B, Figure 4-
185 figure supplement 1A), suggesting a different scenario than deafferentation due to excitotoxic
186 synaptopathy as recently reported (Moverman et al., 2023). Nevertheless, nearly all traced
187 radial fibers were found predominantly unbranched in both the RTN4RL2$^{-/-}$ (97%) and the
188 wild-type control mice (94%; Figure 4F).

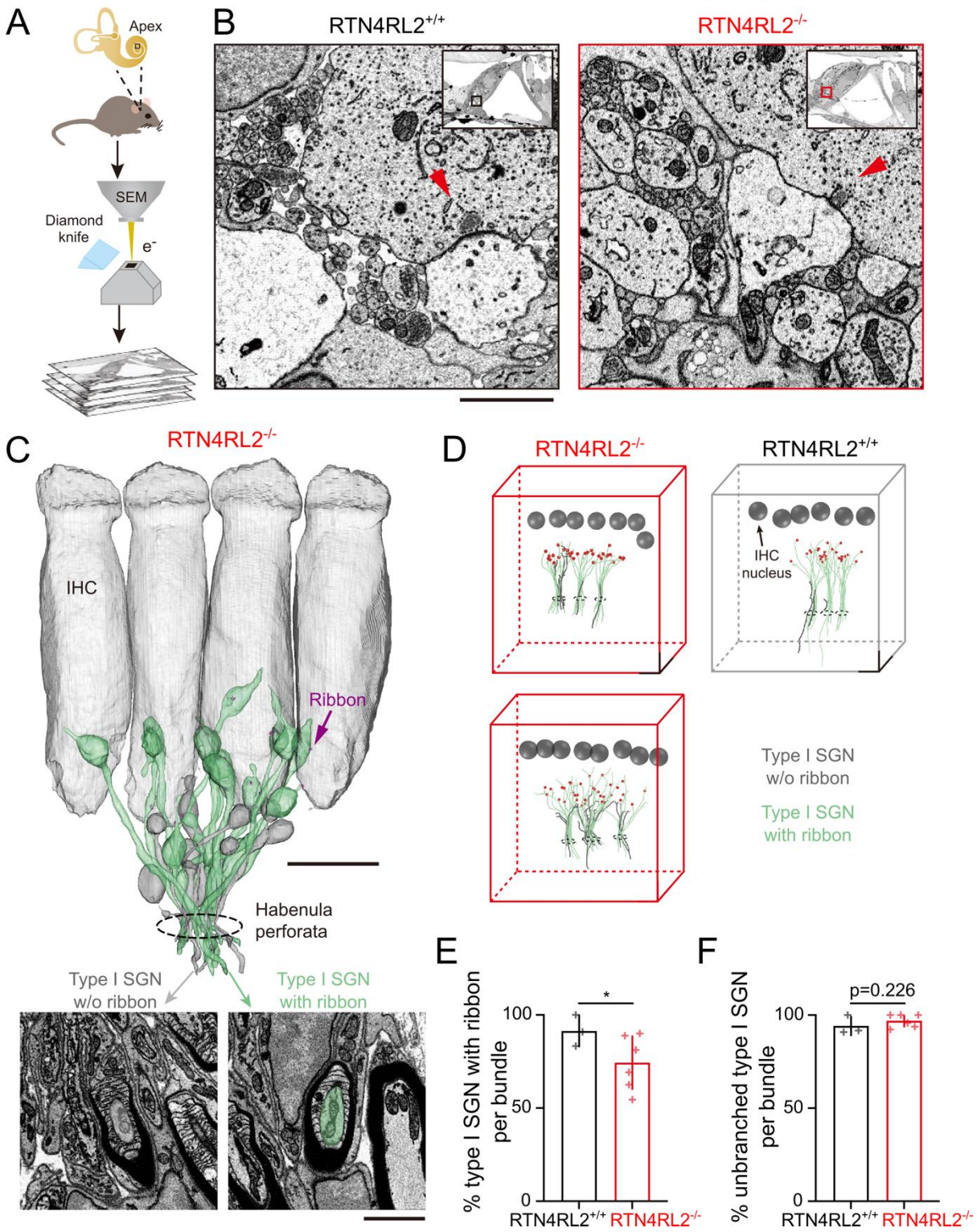

Figure 4. Additional non-synaptically engaged SGN neurites in the cochlea of RTN4RL2$^{-/-}$ mice. (**A**) Workflow of SBEM imaging at the mouse apical cochlear region. (**B**) Example images of neurites beneath IHCs from the RTN4RL2$^{+/+}$ (left) and RTN4RL2$^{-/-}$ (right) mice. Synaptic ribbons are indicated with red arrows. The regions of interest were magnified from single sections of SBEM datasets (insets). Scale bar = 2 µm. (**C**) 3D rendering of afferent fiber reconstruction with ribbons (red), showing both synaptic (green, type I SGN with ribbon) and non-synaptic (grey, type I SGN without ribbon) populations in the RTN4RL2$^{-/-}$ mouse. Scale bar = 10 µm. Inset: EM images show the SGN segments on which myelin sheaths start to form.

198 Scale bar 2 = µm. (**D**) Display of classified radial fibers in the RTN4RL2$^{+/+}$ (right) and RTN4RL2^{-}
199 $^{/-}$ (left and bottom) animals. All fibers were traced from the habenula perforata (cycles) before
200 classification to avoid bias to terminal types. Scale bar = 10 µm. (**E**) Percentage of radial fibers
201 with ribbon per bundle (RTN4RL2$^{+/+}$: 91.41 ± 8.35 %, n = 3 bundles, N = 1 vs RTN4RL2$^{-/-}$: 74.40
202 ± 14.58%, n = 6 bundles, N = 2; p = 0.032, unpaired t-test). (**F**) Percentage of unbranched radial
203 fibers per bundle (RTN4RL2$^{+/+}$: 94.19 ± 5.04 %, n = 3 bundles, N = 1 vs RTN4RL2$^{-/-}$: 96.98 ± 3.49
204 %, n = 6 bundles, N = 2; p = 0.226, unpaired t-test).
205
206 ## Deletion of RTN4RL2 results in depolarized shift of the Ca^{2+} channel activation in IHCs
207
208 Next, we tested for potential effects of RTN4RL2 deletion on the presynaptic IHC function. We
209 performed whole-cell patch-clamp recordings from IHCs of p21-29 RTN4RL2$^{+/+}$ and RTN4RL2^{-}
210 $^{/-}$ mice. First, we recorded voltage-gated Ca^{2+} currents by applying step depolarizations with 5
211 mV increment in ruptured patch-clamp configuration (Figure 5A, see Materials and Methods).
212 We did not observe any change in the maximal Ca^{2+} current amplitude (Figure 5B, C), yet
213 noticed small (~ +3 mV) but consistent and statistically significant depolarized shift of the
214 voltage of half-maximal Ca^{2+} channel activation (V_{half}; Figure 5D, E). The voltage sensitivity of
215 the channels was not changed in RTN4RL2$^{-/-}$ IHCs (Figure 5F). Next, we probed Ca^{2+} influx
216 triggered exocytosis from IHCs by applying depolarizations of varying durations to voltages
217 saturating Ca^{2+} influx in IHCs of both genotypes (-17 mV) and recording exocytic membrane
218 capacitance changes (ΔC_m) in the perforated patch-clamp configuration (Figure 5G). Both fast
219 (up to 20 ms depolarization) and sustained components of exocytosis remained intact in the
220 mutant, indicating unaffected readily releasable pool and replenishment of the vesicles in
221 RTN4RL2$^{-/-}$ IHCs (Figure 5H).

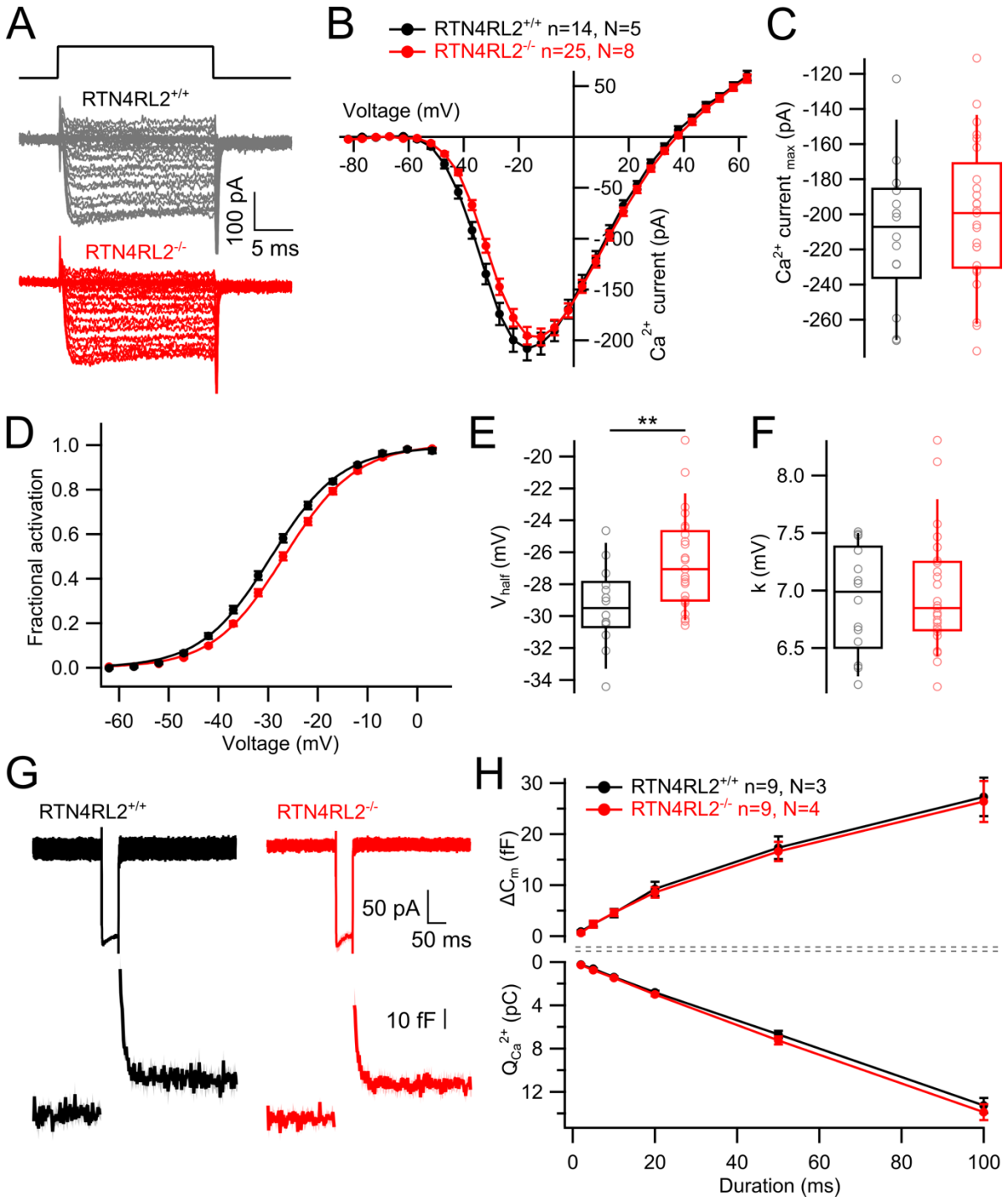

Figure 5. Shifted operation range of Ca^{2+} channels but intact exocytosis in IHCs of RTN4RL2$^{-/-}$ mice. (**A**) Representative current traces from IHCs of RTN4RL2$^{+/+}$ (top, black) and RTN4RL2$^{+/+}$ (bottom, red) evoked by step depolarizations. (**B**) Average Ca^{2+} current-voltage relationships (IV curves) in RTN4RL2$^{+/+}$ and RTN4RL2$^{-/-}$ IHCs. (**C**) Maximal Ca^{2+} current amplitude is not changed in RTN4RL2$^{-/-}$ IHCs (RTN4RL2$^{+/+}$: 210 ± 10.9 pA, SD = 40.9 pA, n = 14, N = 5 vs RTN4RL2$^{-/-}$: -200 ± 8.19 pA, SD = 40.9 pA, n = 25, N = 8; p = 0.47, Student's t-test). (**D**) Fractional activation curves of Ca^{2+} channels calculated from IVs show depolarized shift in channel activation in RTN4RL2$^{-/-}$ IHCs. (**E**) Voltage of half maximal activation obtained from Boltzmann fit of the curves from (D) is more positive in RTN4RL2$^{-/-}$ IHCs (RTN4RL2$^{+/+}$: -29.4 ± 0.66 mV, SD

= 2.48 mV, n = 14, N = 5 vs RTN4RL2$^{-/-}$: -26.6 ± 0.59 mV, SD = 2.94 mV, n = 25, N = 8; p = 0.004, Student's t-test). (**F**) Voltage sensitivity (k) is not changed in RTN4RL2$^{-/-}$ IHCs (RTN4RL2$^{+/+}$: 6.92 ± 0.12 mV, SD = 0.46 mV, n = 14, N = 5 vs RTN4RL2$^{-/-}$: 6.98 ± 0.1 mV, SD = 0.51 mV, n = 25, N = 8; p = 0.93, Mann-Whitney-Wilcoxon test). (**G**) Average current traces evoked by 50 ms depolarization to -17 mV (top row) and resulting capacitance response (bottom row) from RTN4RL2$^{+/+}$ (left, black) and RTN4RL2$^{+/+}$ (right, red) IHCs. Shaded areas represent ± SEM. (**H**) Exocytic capacitance change (ΔC_m, top) and corresponding Ca^{2+} charge (Q_{Ca}^{2+}, bottom) evoked by depolarizations (to -17 mV) of various durations (2, 5, 10, 20, 50, 100 ms). Box-whisker plots show the median, 25/75 percentiles (box) and 10/90 percentiles (whiskers). Individual data points are overlaid.

We then turned to study single AZ function by combining whole cell ruptured patch-clamp with spinning disc confocal imaging of presynaptic Ca^{2+} influx, as described previously (Ohn et al., 2016). TAMRA conjugated Ctbp2 binding dimeric peptide and the low affinity Ca^{2+} indicator Fluo4-FF (k_D: 10 µM) were loaded into the cell via the patch pipette and Ca^{2+} influx at single AZs was visualized in the form of hotspots by applying voltage ramp depolarizations to the IHCs and simultaneously imaging Fluo4-FF fluorescence near labeled ribbons (Figure 6A, see Materials and methods). Maximal Ca^{2+} influx at single AZs tended to be higher in IHCs of RTN4RL2$^{-/-}$ mice but the difference did not reach statistical significance (Figure 6B, B^{i}). The V_{half} of Ca^{2+} channel clusters at single AZs showed depolarized shift (~ +5 mV), which was statistically significant despite the large variability of V_{half} across different AZs (Figure 6C, C^{i}). Furthermore, we did not observe any mismatch in Ctbp2 positive puncta and evoked Ca^{2+} hotspots, indicating the correct localization of Ca^{2+} channels at the AZs. We verified this by performing immunostainings of $Ca_V1.3$, Ctbp2 and Bassoon and did not detect any apparent misalignment of these protein clusters (Figure 6D). In summary, deletion of RTN4RL2 causes a depolarized shift of the activation of presynaptic Ca^{2+} influx in IHCs as demonstrated at the single AZ and whole cell levels. This is expected to elevate the sound pressure levels required to reach a comparable activity of synaptic transmission for sound encoding and predicts elevated auditory thresholds which we tested by recordings of auditory brainstem responses.

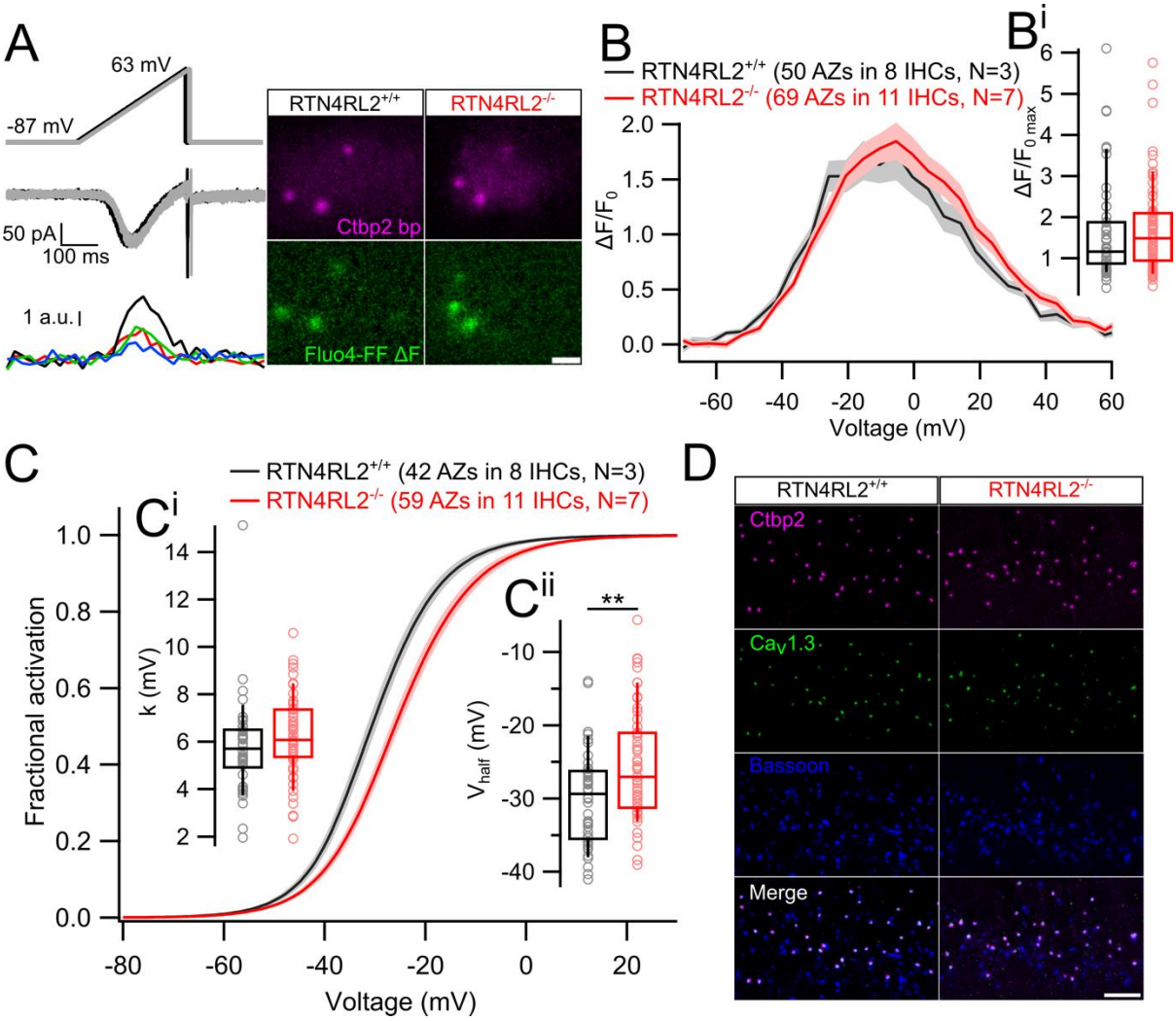

Figure 6. Depolarized shift of Ca^{2+} channel activation at single AZs but intact presynaptic organization in RTN4RL2$^{-/-}$ IHCs. (**A**) Voltage ramp stimulation protocols (top), evoked whole cell currents (middle) and the presynaptic hotspots of Fluo4-FF fluorescence (bottom) of a representative IHC recording. Black and grey colors represent the two stimulations, one being 5 ms shifted over the other. Images on the right show single imaging planes of representative RTN4RL2$^{+/+}$ (left) and RTN4RL2$^{-/-}$ (right) IHCs filled with TAMRA conjugated Ctbp2 binding peptide (Ctbp2 bp) and Fluo4-FF Ca^{2+} dye. Ca^{2+} hotspots are visualized by subtracting the average of baseline planes from the average of 5 planes during stimulation. Scale bar = 2 µm. (**B**) Average fluorescence-voltage relationships of Ca^{2+} influx at single AZ from RTN4RL2$^{+/+}$ and RTN4RL2$^{-/-}$ IHCs show no difference in the maximal Ca^{2+} amplitude (**B^{i}**; RTN4RL2$^{+/+}$: 1.6 ± 0.17, SD = 1.2, n = 50 AZs vs RTN4RL2$^{-/-}$: 1.7 ± 0.13 pA, SD = 1.09, n = 69 AZs; p = 0.24, Mann-Whitney-Wilcoxon test). Shaded areas represent ± SEM. (**C**) Average fractional activation curves of Ca^{2+} channels at single AZs show intact voltage sensitivity (**C^{i}**; RTN4RL2$^{+/+}$: 5.79 ± 0.32 mV, SD = 2.04 mV, n = 42 AZs vs RTN4RL2$^{-/-}$: 6.25 ± 0.22 mV, SD = 1.7 mV, n = 59 AZs; p = 0.06, Mann-Whitney-Wilcoxon test) but depolarized shift of V_{half} (**C^{ii}**; RTN4RL2$^{+/+}$: -30 ± 1 mV, SD = 6.5 mV, n = 42 AZs vs RTN4RL2$^{-/-}$: -25.5 ± 0.98 mV, SD = 7.49 mV, n = 59 AZs; p = 0.002, Student's t-test) in RTN4RL2$^{-/-}$ IHCs. Shaded areas represent ± SEM. (**D**) Representative immunolabelings of presynaptic proteins show no apparent mislocalization in RTN4RL2$^{-/-}$ IHCs. Scale bar = 5 µm. Box-whisker plots show the median, 25/75 percentiles (box) and 10/90 percentiles (whiskers). Individual data points are overlaid.

RTN4RL2 is essential for normal hearing

In order to evaluate auditory systems function in RTN4RL2$^{-/-}$ mice, we recorded auditory brainstem responses (ABRs) at the age of 2-4 months. ABRs were elicited in response to 4, 8, 16, 32 kHz tone bursts and click stimuli of increasing sound pressure levels. We determined the sound thresholds by identifying the lowest sound pressure level which resulted in detectable ABR waveform. We found ABR thresholds to be significantly increased by around 30-45 dB across all the tested frequencies and in response to the click stimulations in RTN4RL2$^{-/-}$ mice compared to the wild-type controls (Figure 7). RTN4RL2$^{+/-}$ mice showed an intermediate phenotype between the RTN4RL2$^{-/-}$ and RTN4RL2$^{+/+}$ mice with a lower yet significant increase of ABR thresholds of approximately 10-15 dB at 4, 16 and 32 kHz frequencies.

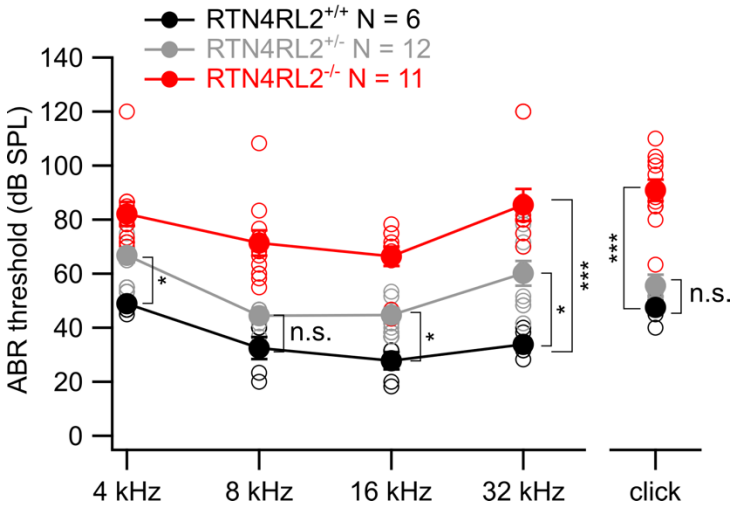

Figure 7. Elevated acoustic thresholds in RTN4RL2$^{-/-}$ mice. ABR thresholds were measured in response to 4, 8, 16, 32 kHz tone bursts and click stimuli. ABR thresholds of individual animals are shown in open circles on top of the mean ± SEM. Statistical significances are reported as *p < 0.05, ***p < 0.001, Kruskal-Wallis followed by Dunn's multiple comparison test.

Discussion

In this study, we investigated the role of the Nogo/RTN4 receptor homolog RTN4RL2 in the cochlea. Consistent with the previous reports, we detected RTN4RL2 expression in IHCs and SGNs. Upon RTN4RL2 deletion, we observed alterations of the IHC-SGN synapses (Figure 8). Presynaptically, Ca^{2+} channel activation was shifted towards depolarized voltages and ribbon size was enlarged. IHC exocytosis was unaltered when probed at saturating depolarizations. At the postsynaptic side, PSDs juxtaposing presynaptic ribbons were smaller compared to the

controls and seemed to be deficient of GluA2-4, despite the expression of Gria2 mRNA in RTN4RL2$^{-/-}$ SGNs. Additionally, we observed PSDs which resided further from the IHC membrane and did not juxtapose the presynaptic AZs in RTN4RL2$^{-/-}$ mice. These PSDs potentially belong to the type I SGN neurites that ended in the inner spiral bundle without contacting the IHCs, as observed in SBEM reconstructions of RTN4RL2$^{-/-}$ SGNs. Finally, ABR thresholds were elevated in RTN4RL2$^{-/-}$ mice indicating that RTN4RL2 is required for normal hearing.

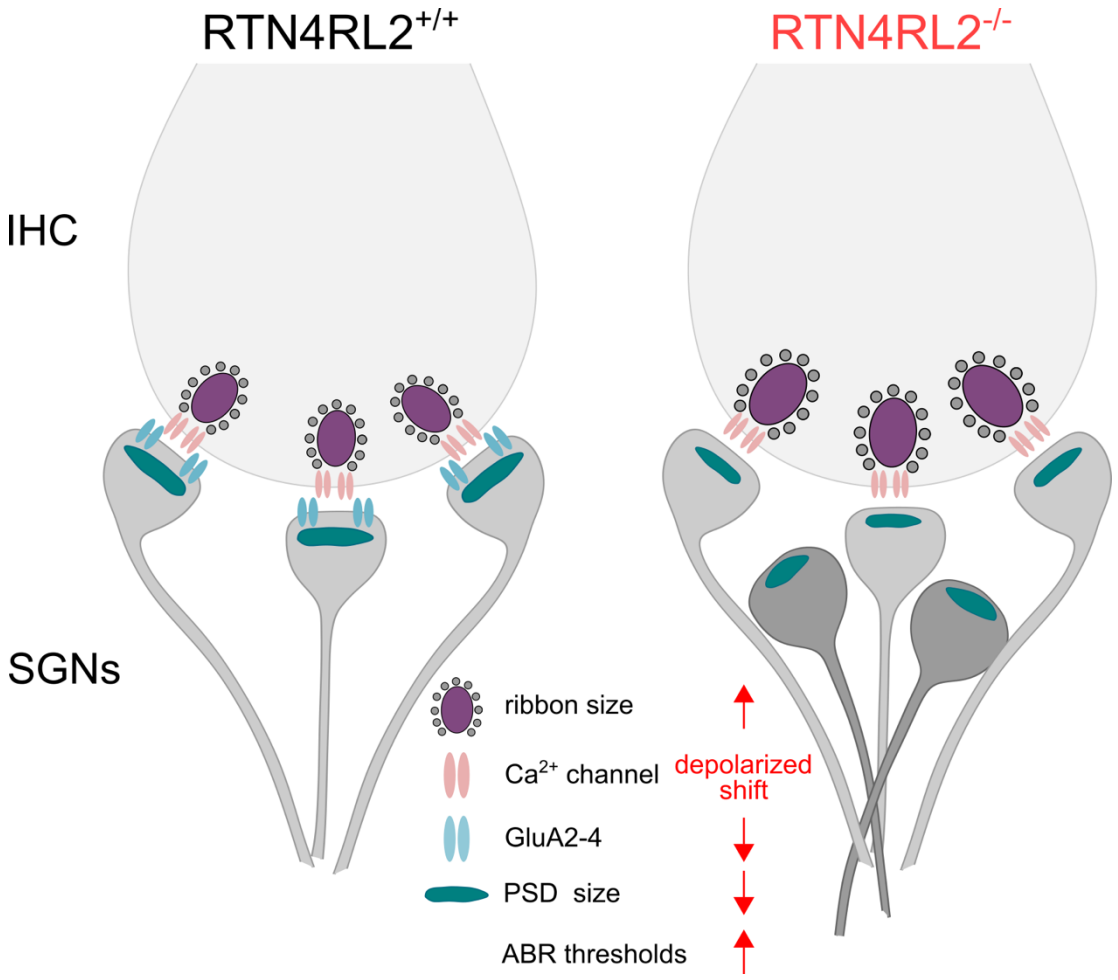

Figure 8. Schematic illustration of the key structural and functional changes in the auditory periphery of RTN4RL2$^{-/-}$ mice. RTN4RL2$^{-/-}$ mice display enlarged synaptic ribbons and depolarized shift in the activation of presynaptic Ca^{2+} channels in IHCs, as well as reduced size of PSDs juxtaposing presynaptic ribbons. RTN4RL2 deficiency further leads to a decrease in GluA2-4 AMPA receptor subunits at PSDs and results in a subset of type I SGN neurites that reach the inner spiral bundle but do not engage the IHCs.

RTN4 receptors have been implicated as presynaptic adhesion molecules based on their transsynaptic interactions with postsynaptically enriched brain-specific angiogenesis inhibitor

326 (BAI) adhesion GPCRs (Stephenson et al., 2013; Wang et al., 2021). Despite this, at least RTN4R
327 has been proposed to function postsynaptically, given that its knockdown leads primarily to
328 postsynaptic changes (Wills et al., 2012). The interpretation of RTN4R function and localization
329 is further complicated by their enrichment in both pre- and postsynaptic terminals (Wang et
330 al., 2002b). Similarly, we observed RTN4RL2 expression in both IHCs and SGNs. Interestingly,
331 a recent study described a hearing impairment in BAI1 deficient mice and suggested that
332 postsynaptically functioning BAI1 is important for correct localization of AMPA receptor
333 subunits in spiral ganglion neurons based on the absence or decrease of different AMPA
334 receptor subunits at the SGN postsynapses in BAI1 deficient mice (Carlton et al., 2024).
335 Similarly, our data from RTN4RL2$^{-/-}$ mice show the absence of GluA2-4 positive puncta
336 juxtaposing presynaptic AZs. Importantly, the BAI1 knock-out model in the study by Carlton et
337 al. eliminated specifically long isoform of BAI1, which contains extracellular thrombospondin
338 repeats (TSRs) important for mediating transsynaptic interactions, while leaving she short
339 isoform - containing the transmembrane repeats and intracellular domain of the receptor -
340 intact (Wang et al., 2021; Carlton et al., 2024). Along with the evidence for transsynaptic
341 interaction between RTN4Rs and BAIs (Wang et al., 2021), this raises the possibility that the
342 GluA2-4 AMPA receptor subunit localization to SGN PSDs requires the interaction of
343 presynaptic RTN4RL2 and postsynaptic BAI1. Likewise, the changes of presynaptic Ca^{2+}
344 channel properties and ribbons in IHCs could result from direct presynaptic action of RTN4RL2.
345 Alternatively, RTN4RL2 could act postsynaptically in SGNs with an impact on transsynaptic
346 signaling to IHCs. Presynaptic changes upon postsynaptic manipulation have been reported
347 previously. For instance, the deletion of postsynaptically expressed Pou4f1 transcription factor
348 resulted in hyperpolarized shift of IHC Ca^{2+} channels, as well as in changes of the presynaptic
349 heterogeneity of IHC AZs (Sherrill et al., 2019). Similarly, presynaptic ribbon sizes were altered
350 in IHCs of mice, which exhibited conditional deletion of Runx1 transcription factor from SGNs
351 (Shrestha et al., 2023). Further experiments, employing mouse mutants with specific RTN4RL2
352 deletion in IHCs or SGNs will allow to evaluate the precise presynaptic and postsynaptic roles
353 of RTN4RL2 including a possible transsynaptic signaling to IHC AZs.

354 We propose that the afferent synaptic changes contribute to the severe hearing
355 impairment in RTN4RL2$^{-/-}$ mice. The phenotype of increased ABR thresholds could partially be
356 explained by the depolarized activation of Ca^{2+} channels in IHCs. As it has been shown, the
357 apparent Ca^{2+} dependence of glutamate release from IHCs on average follows a near linear

358 relationship (Wong et al., 2014; Özçete and Moser, 2021; Jaime Tobón and Moser, 2023b,
359 2023a). Therefore, due to the depolarized shift of the Ca^{2+} channel activation, the glutamate
360 release from IHCs would require stronger stimuli. While exocytosis, probed by depolarizing
361 the IHCs to -17 mV and recording cell membrane capacitance changes, remained intact in
362 RTN4RL2$^{-/-}$ mice, it could still be affected at milder depolarizations (e.g., -50 mV to -40 mV),
363 which correspond to the receptor potential range of the IHCs. This could result in increased
364 sound thresholds, as shown in Ribeye knock-out mice, where depolarized activation of Ca^{2+}
365 channels has been associated with higher firing thresholds and lower spontaneous rates in
366 SGNs, although a less severe hearing phenotype was observed in those mice (Jean et al.,
367 2018). Furthermore, we have shown recently that a direct manipulation of the voltage
368 dependence of $Ca_v1.3$ Ca^{2+} channel activation results in changes of SGN firing and potentially
369 auditory thresholds, further supporting our hypothesis of sound threshold elevation in
370 RTN4RL2$^{-/-}$ mice being caused by the depolarized activation of Ca^{2+} channels in IHCs
371 (Karagulyan et al., 2025).
372 In addition or alternatively, the increase in auditory thresholds could be caused by the
373 deficiency of GluA2-4 AMPA receptors of the SGN postsynapses in RTN4RL2$^{-/-}$ mice. Compared
374 to GluA3 KO mice, which display reduced GluA2 signal at SGN PSDs but intact auditory
375 thresholds, the increased auditory thresholds in RTN4RL2$^{-/-}$ mice could additionally be caused
376 by the lack of GluA4 subunits juxtaposing presynaptic ribbons, which, in contrast, were shown
377 to be upregulated in GluA3 KO mice (Rutherford et al., 2023). Given the observed synaptic
378 changes, it seems less likely that the hearing impairment would have resulted from the
379 intrinsic changes of SGN firing. Further experiments, where SGNs would be stimulated directly
380 via *ex vivo* patch-clamp or optogenetically could help to probe for functional deficits in SGNs
381 of RTN4RL2$^{-/-}$ mice. Another interesting observation was the additional PSDs not juxtaposing
382 presynaptic ribbons that were detected around IHCs of RTN4RL2$^{-/-}$ mice. These “orphan” PSDs
383 seem not to be part of the efferent synapses formed between LOC/MOCs and SGNs as we
384 verified by simultaneous anti-Homer1 and anti-synapsin immunolabelings. To check the SGN
385 connectivity we performed SBEM in RTN4RL2$^{+/+}$ and RTN4RL2$^{-/-}$ cochlear samples and
386 observed a high percentage of non-synaptic SGN neurites in the reconstructed neurons of
387 inner spiral bundles in RTN4RL2$^{-/-}$ samples. A sizable subset of the non-synaptic SGN boutons
388 did not make a contact with IHCs, potentially housing the “orphan” PSDs observed around the
389 IHCs in our immunolabeled samples. How exactly those non-synaptic neurites appear remains

390 to be investigated. SGN neurite retraction from IHCs has been demonstrated in noise-exposed
391 animals, followed by the degeneration of the SGN somata and axons (Kujawa and Liberman,
392 2009, 2015; Moverman et al., 2023). This process however results in up to 50% degeneration
393 of the ribbon synapses. Interestingly, in RTN4RL2$^{-/-}$ mice the number of the ribbon synapses
394 as well as the density of the SGN somata was largely intact. This indicates that the non-
395 synaptic neurites do not result from synaptic loss as found in hereditary or acquired
396 synaptopathy (Roux et al., 2006; Ruel et al., 2008; Seal et al., 2008; Kujawa and Liberman,
397 2009). Although it is plausible that the non-synaptic SGN neurites may fail to reach the IHCs
398 during initial development, it is unlikely that this would selectively impact only a subset of
399 neurons and still allow the Homer1-positive patches to develop in the absence of presynaptic
400 components. Alternatively, it is known that major synaptic pruning takes place in developing
401 SGNs, whereby up to 50% of the synapses are lost between the IHCs and the SGNs (Defourny
402 et al., 2013; Coate et al., 2019), suggesting that the non-synaptic SGN neurites of RTN4RL2$^{-/-}$
403 mice could be a result of failed pruning of SGNs during the development. Yet how this would
404 then comply with normal synapse and SGN counts remains to be elucidated. Future studies
405 will be required to understand the fate of type I SGNs in RTN4RL2$^{-/-}$ mice during development
406 by mapping their full-length periphery projections with large scale imaging tools.
407 Future work will be required to identify the RTN4RL2 ligands in the cochlea. To this
408 date, the interaction partners of RTN4Rs are not very well understood. While RTN4R in-trans
409 interactions include NogoA, MAG, OMgp, chondroitin sulfate proteoglycans, the only well
410 established ligand for RTN4RL2 remains MAG (Fournier et al., 2001; Domeniconi et al., 2002;
411 Wang et al., 2002a; Venkatesh et al., 2005; Schwab, 2010). Other attractive candidate ligands
412 for RTN4Rs are the BAIs. BAI-RTN4R interaction has been suggested to mediate dendritic
413 arborization, axonal elongation, synapse formation in IPSCs (Wang et al., 2021) and, in the
414 case of this study GluA2-4 AMPA receptor subunit localization to the SGN postsynaptic
415 densities. Finally, RTN4RL2 has been proposed to interact with chondroitin-sulfate
416 proteoglycan Versican to control the amount of skin innervation by DRG neurites (Bäumer et
417 al., 2014). While to our knowledge, attempts have yet to be made for detecting Versican signal
418 around the IHCs, other extracellular matrix proteins such as aggrecan, brevican, Tenascin-R,
419 Tenascin-C, hyaluron and proteoglycan link proteins 1 and 4 have been shown to form dense,
420 basket-like structures that surround the base of the IHCs (Kwiatkowska et al., 2016; Sonntag
421 et al., 2018). Furthermore, deletion of brevican results in alteration of pre- and postsynaptic

spatial coupling at IHC synapses, indicating the possible role of extracellular matrix in transsynaptic organization. However, while the existing observations suggest that the synaptic changes in RTN4RL2 deficient animals might reflect derailed interaction of the SGN neurites with the extracellular matrix, the relevance of such an interaction of RTN4RL2 and Versican in the cochlea needs to be addressed in the future.

Materials and Methods

Animals

RTN4RL2 null mutant mice on a C57BL/6N background were generated as previously described (Wörter et al., 2009). Knock-out (RTN4RL2$^{-/-}$) and wild-type (RTN4RL2$^{+/+}$) mice were derived from heterozygous matings. Both male and female mice were used in this study. Animals were genotyped as previously described (Wörter et al., 2009). The ages of the mice varied depending on the experiment as noted in the manuscript. The breeding and the experiments were approved by the Institutional Animal Care and Use Committee at the Medical University of Innsbruck, local Animal Welfare Committee of the University Medical Center Göttingen and the Max Planck Institute for Multidisciplinary Sciences, as well as the Animal Welfare Office of the state of Lower Saxony, Germany (LAVES, AZ: 19/3134). The ABR experiments were carried out under the approval of the Austrian Ministry of Education, Science and Research (reference number BMWFW-66.011/0120-WF/V/3b/2016).

Patch-clamp recordings

The apical turn of the organ of Corti was dissected from p21 to p29 animals in HEPES Hanks solution containing (in mM): 5.36 KCl, 141.7 NaCl, 10 HEPES, 0.5 $MgSO_4$, 1 $MgCl_2$, 5.6 D-glucose, and 3.4 L-glutamine (pH 7.2, ~ 300 mOsm/l). IHCs were exposed by gently removing of nearby supporting cells by negative pressure through a glass pipette from either modiolar or pillar side. All experiments were conducted at room temperature (RT, 20–25°C). Patch pipettes were made from GB150-8P or GB150F-8P borosilicate glass capillaries (Science Products, Hofheim, Germany) for perforated and ruptured patch-clamp configurations, respectively. Pipettes were fire polished with a custom-made microforge and coated with Sylgard to minimize the capacitive noise, whenever capacitance recordings were performed. The measurements were performed using EPC-10 amplifier controlled by Patchmaster software (HEKA Elektronik, Germany). The holding potential for IHCs was set to -87 mV across all the experiments.

Ruptured patch-clamp

460 For ruptured patch-clamp we used extracellular solution containing (in mM): 2.8 KCl, 105 NaCl,
461 10 HEPES, 1 CsCl, 1 $MgCl_2$, 5 $CaCl_2$, 35 TEA-Cl, and 2 mg/ml D-glucose (pH 7.2, ~ 300 mOsm/l).
462 Intracellular solution contained in mM: 111 Cs-glutamate, 1 $MgCl_2$, 1 $CaCl_2$, 10 EGTA, 13 TEA-
463 Cl, 20 HEPES, 4 Mg-ATP, 0.3 Na-GTP and 1 L-glutathione (pH 7.3, ~ 290 mOsm/l). Additionally,
464 Ca^{2+} indicator Fluo4-FF (0.8 mM, Life Technologies) and TAMRA-conjugated RIBEYE/Ctbp2
465 binding peptide (10 mM, synthetized by the group of Dr. Olaf Jahn, Göttingen) were added to
466 the intracellular solution for live imaging (Zenisek et al., 2004). Voltage dependency of Ca^{2+}
467 influx was recorded by applying 20 ms long step deploarizations with 5 mV increment. For
468 Ca^{2+} imaging, voltage ramp depolarizations ranging from -87 mV to 63 mV in the course of 150
469 ms were applied to the cells. Leak correction was performed using p/4 protocol and liquid
470 junction potential of 17 mV was corrected offline. Recordings were discarded from the
471 analysis if the series resistance (R_s) exceeded 14 MOhm during the first 3 minutes after
472 rupturing the cell, leak current exceeded -50 pA at the holding potential and Ca^{2+} current
473 rundown was more than 25%.
474 Recordings were analyzed using Igor Pro 6.3 (Wavemetrics) custom-written programs. Ca^{2+}
475 current-voltage relationships (IV curves) were obtained by averaging approximately 5 ms
476 segments at the maximal activation regions of individual current traces and plotting them
477 against the depolarization voltages. Fractional activation curves of the Ca^{2+} channels were
478 calculated from the IVs, normalized and fitted with the Boltzmann function: $G/G_{max} =$
479 $\frac{1}{1+\exp\left[\frac{V_m - V_{half}}{k}\right]}$, where G is conductance, G_{max} is the maximal conductance, V_m is the
480 membrane potential, V_{half} is the voltage corresponding to the half maximal activation of Ca^{2+}
481 channels and k (slope of the curve) is the voltage sensitivity of Ca^{2+} channel activation.
482

483 ## Perforated patch clamp recordings
484

485 To perform simultaneous membrane capacitance (C_m) and Ca^{2+} current measurements we
486 used extracellular solution containing (in mM): 106 NaCl, 35 TEA-Cl, 2.8 KCl, 1 $MgCl_2$, 1 CsCl,
487 10 HEPES, 3 $CaCl_2$, and 5.6 D-glucose (pH 7.2, ~ 300 mOsm/l). The pipette solution contained
488 (in mM): 137 Cs-gluconate, 15 TEA-Cl, 3 GTP-Na_2, 1 ATP-Mg, 10 HEPES, 1 $MgCl_2$, as well as 300
489 mg/ml amphotericin B (pH 7.17, ~ 290 mOsm/l). Perforated patch-clamp recordings from
490 IHCs were described previously (Moser and Beutner, 2000). C_m changes were measured using

491 Lindau-Neher technique (Lindau and Neher, 1988). To evoke exocytosis IHCs were stimulated
492 by step depolarizations (to -17 mV) of different durations (2, 5, 10, 20, 50, 100 ms) in
493 randomized manner. Currents were leak-corrected using a p/5 protocol. Recordings were used
494 only if the leak current was lower than 30 pA and the R_s was lower than 30 MOhm. Recordings
495 were analyzed using Igor Pro 6.3 (Wavemetrics) custom-written programs. Ca^{2+} charge (Q_{Ca}^{2+})
496 was calculated by the time integral of the leak-subtracted Ca^{2+} current during the
497 depolarization step. ΔC_m was calculated as the difference between the average C_m before and
498 after the depolarization. To measure average C_m we used 400 ms segments and skipped the
499 initial 100 ms after the depolarization.

500

501 ## Ca^{2+} imaging

502

503 Ca^{2+} imaging was performed using spinning disc confocal microscope, as described before
504 (Ohn et al., 2016). Briefly, the set-up was equipped with a spinning disc confocal unit (CSU22,
505 Yokogawa) mounted on an upright microscope (Axio Examiner, Zeiss) and scientific CMOS
506 camera (Andor Neo). Images were acquired using 63x, 1.0 NA objective (W Plan-Apochromat,
507 Zeiss). The pixel size was measured to be 103 nm.
508 IHCs were loaded with Fluo4-FF Ca^{2+} dye and TAMRA-conjugated Ctbp2 binding dimeric
509 peptide via the patch pipette. First, the cells were scanned from bottom to top by imaging
510 TAMRA fluorescence with 561 nm laser (Jive, Cobolt AB) and exposing each plane for 0.5
511 seconds. The stack was acquired with 0.5 μm step size using Piezo positioner (Piezosystem).
512 This allowed us to identify the planes containing synaptic ribbons. Next, we recorded Fluo4-
513 FF fluorescence increase at individual synapses by imaging ribbon containing planes with 491
514 nm laser (Calypso, Cobolt AB) at 100 Hz while applying voltage ramp depolarizations to the
515 cell. 2 voltage ramps were applied at each plane, one being 5 ms shifted relative to the other.
516 Spinning disk rotation speed was set to 2000 rpm, in order to synchronize with Ca^{2+} imaging.
517 Images were analyzed using Igor Pro 6.3 (Wavemetrics). Ca^{2+} hotspots were identified by
518 subtracting the average signal of several baseline frames from the average signal of 5 frames
519 during stimulation (ΔF image). Since the same Ca^{2+} hotspot appears across multiple planes,
520 the plane exhibiting the strongest signal was chosen. The intensities of the 3x3 matrix
521 surrounding the central pixel of the hotspot were averaged across all time points to obtain the
522 intensity profiles of Ca^{2+} influx over time. Afterwards, the background signal (average of

523 approximately 60x60 pixel intensities outside the cell) was subtracted from the intensity-time
524 profiles and $\Delta F/F_0$ traces were calculated. To enhance voltage resolution of Ca^{2+} imaging, two
525 $\Delta F/F_0$ traces corresponding to two voltage ramp depolarizations (one shifted by 5 ms over the
526 other) were combined and plotted against the corresponding voltages (FV curves). These
527 curves were subsequently fitted with a modified Boltzmann function. Afterwards, fractional
528 activation curves were calculated by fitting the linear decay of the fluorescence signal from
529 the FV curves with a linear function (G_{max}) and then dividing the FV fit by the G_{max} line. The
530 resulting curves were further fitted with a Boltzmann function. Maximal Ca^{2+} influx ($\Delta F/F_{0\ max}$)
531 was calculated by averaging 5 points during the stimulation.
532
533 ## Immunohistochemistry
534
535 For whole mount immunofluorescence, cochleae were fixed in 4% formaldehyde on ice for
536 45-60 minutes or sometimes overnight. For anti-$Ca_V1.3$ stainings the cochleae were fixed for
537 10 minutes. After the fixation, the organs of Corti were microdissected in PBS and blocked in
538 GSDB (goat serum dilution buffer; 16% goat serum, 20 mM phosphate buffer (PB), 0.3% Triton
539 X-100, 0.45 M NaCl) for 1 hour at RT. The samples were then incubated in the primary antibody
540 mixture overnight at 4°C. For anti-GluA4 immunolabelings samples were incubated at primary
541 antibody mixture at 37°C overnight. The next day, samples were washed 3 times using wash
542 buffer (20 mM PB, 0.3% Triton X-100, 0.45 M NaCl) followed by incubation in the secondary
543 antibody mixture for 1 hour at RT. Afterwards, the samples were washed 3 times in the
544 washing buffer, one time in PB and mounted using mounting medium (Mowiol).
545 The following primary antibodies were used (Table 1): rabbit anti-Homer1 (1:500, 160 002,
546 Synaptic Systems), mouse anti-Ctbp2 (1:200, 612044, BD Biosciences), rabbit anti-$Ca_V1.3$
547 (1:100, ACC-005, Alomone Labs), mouse anti-Bassoon (1:300, ab82958, Abcam), mouse anti
548 GluA2 (1:200, MAB397, Millipore), rabbit anti GluA4 (1:200, AB1508, Millipore), rabbit anti
549 GluA2/3 (1:200, AB1506, Chemicon), rabbit anti-Myosin7a (1:800, ab3481, Abcam, or Proteus
550 BioSciences), guinea pig anti-RibeyeA (1:500, 192104, Synaptic Systems), guinea pig anti-
551 Synapsin1/2 (1:500, 106004, Synaptic Systems), guinea pig anti-Vglut3 (1:500, 135204,
552 Synaptic Systems), chicken anti-parvalbumin (1:200, 195006, Synaptic Systems), chicken anti-
553 calretinin (1:200, 214106, Synaptic Systems), guinea pig anti-VAChT (1:1000, 139105, Synaptic
554 Systems), mouse anti-ATP1A3 (1:300, MA3-915, Thermo Fisher Scientific).

555 The following secondary antibodies were used: Alexa Fluor 488 conjugated anti-guinea pig
556 (1:200, A11073, Thermo Fisher Scientific), Alexa Fluor 488 conjugated anti-rabbit (1:200,
557 A11008, Thermo Fisher Scientific), Alexa Fluor 568 conjugated anti-chicken (1:200, ab175711,
558 Abcam), Alexa Fluor 633 conjugated anti-guinea pig (1:200, A21105, Thermo Fisher Scientific),
559 STAR 580 conjugated anti-mouse (1:200, Abberior, ST635P-1001-500UG), STAR 635
560 conjugated anti-rabbit (1:200, Abberior, ST635P-1002-500UG).
561 Confocal stacks were acquired using Leica SP8 confocal microscope or Abberior Instruments
562 Expert Line STED microscope.
563 The volumes of the Ctbp2 and Homer1 positive puncta were estimated using the surface
564 algorithm of Imaris software (version 9.6.0, Bitplane). Following parameters were used to
565 create the surfaces for both Ctbp2 and Homer1 puncta in all the analyzed stacks: surface detail
566 0.07 µm, background subtraction 0.562 µm, touching object size 0.4 µm.
567 The brightness and the contrast of the representative images were adjusted using Fiji (ImageJ)
568 software for the visualization purposes.

Antibody	**Host species**	**Company**	**Dilution**	**Cat. No.**	**Validation**
anti-Homer1	rabbit	Synaptic Systems	1:500	160002	Refer to manufacturer's datasheet
anti-Ctbp2	mouse	BD Biosciences	1:200	612044	KO validation; DOI: 10.7554/eLife.30241 DOI: 10.7554/eLife.29275
anti-$Ca_V1.3$	rabbit	Alomone Labs	1:100	ACC-005	KO validation; https://doi.org/10.1523/JNEUROSCI.3411-05.2005
anti-Bassoon	mouse	Abcam	1:300	ab8298	Refer to manufacturer's datasheet
anti GluA2	mouse	Millipore	1:200	MAB397	validated for use in ELISA, IC, IH, IP, RIA & WB; Refer to manufacturer's datasheet
anti-GluA2/3	rabbit	Chemicon	1:200	AB1506	validated for use in IH(P), IC, IH, IP, WB; Refer to manufacturer's datasheet
anti GluA4	rabbit	Millipore	1:200	AB1508	KO validation ; DOI: 10.1126/sciadv.aax5936
anti-Myosin7a	rabbit	Abcam/ Proteus BioSciences	1:800	ab3481	Refer to manufacturer's datasheet

anti-RibeyeA	guinea pig	Synaptic Systems	1:500	192104	Refer to manufacturer's datasheet
anti-Synapsin 1/2	guinea pig	Synaptic Systems	1:500,	106004	KO validation; Refer to manufacturer's datasheet
anti-Vglut3	guinea pig	Synaptic Systems	1:500	135204	KO validation; DOI: 10.3389/fncel.2017.00140
anti-Parvalbumin	chicken	Synaptic Systems	1:200	195006	Refer to manufacturer's datasheet
anti-Calretinin	chicken	Synaptic Systems	1:200	214106	Refer to manufacturer's datasheet
anti-VaChT	guinea pig	Synaptic Systems	1:1000	139105	Refer to manufacturer's datasheet
anti-ATP1A3	mouse	Invitrogen	1:300	MA3-915	Refer to manufacturer's datasheet
βIII-tubulin	mouse	Biolegend	1:1000	801202	Refer to manufacturer's datasheet

Table 1. List of primary antibodies.

Spiral ganglion neuron densities

RTN4RL2$^{+/+}$ and RTN4RL2$^{-/-}$ cochlea from p40 mice of either sex were processed for SGN counts. Mouse monoclonal anti-βIII-tubulin (1:1000, 801202, Biolegend) at 4ºC, followed by secondary Alexa Fluor 488 conjugated anti-mouse (1:1000, Thermo Fisher Scientific), was used to label all SGNs. Nuclei were visualized using a DAPI fluorescent counterstain (1:1000, Life Technologies). 20X images of mid-modiolar cochlear sections were collected. ImageJ was used to outline the spiral ganglion and generate the area. Quantitative assessment was performed on every other mid-modiolar section to reduce chances of double counting. Labeled cells were counted only if they had a round cell body, presence of nucleus, and homogenous cytoplasm. Densities were calculated and statistical differences were measure using a Student's t-test (GraphPad Prism, GraphPad Software Inc.).

Inner and outer Hair cell counts

IHC and OHC counts were performed for RTN4RL2$^{+/+}$ and RTN4RL2$^{-/-}$ mice at the ages of p15, 1 month and 2 months. Images were imported to ImageJ software, where IHC/OHC counts were performed blinded to genotype using the 'Cell counter' tool. To quantify the cells the nuclear staining of the DAPI channel was used. The number of IHCs and OHCs was assessed

589 along a length of 100 μm for each image, and then averaged across all samples to obtain the
590 average number of IHCs (or OHCs) per 100 μm.
591
592 ## RNAscope
593
594 RNA *in-situ* hybridization was performed using RNAscope® (Advanced Cell Diagnostics).
595 Standard mouse probes were used to examine the expression of RTN4RL2 (450761, ACD) and
596 Gria2 (865091, ACD) closely following the manufacturer's instructions. Briefly, 6 mm paraffin
597 tissue sections underwent deparaffinization with xylene and a series of ethanol washes.
598 Tissues were heated in kit-provided antigen retrieval buffer and digested by kit-provided
599 proteinase. Sections were exposed to mFISH target probes and incubated at 40°C in a
600 hybridization oven for 2 hours. After rinsing, mFISH signal was amplified using company-
601 provided pre-amplifier and amplifier conjugated to fluorescent dye. Subsequently, sections
602 were blocked with 1% BSA, 2% normal goat serum in 1xPBS containing 0.3% Triton X-100 for
603 1 hour at RT. The tissue was incubated in mouse anti-βIII-tubulin antibody (1:500, 801202,
604 Biolegend) overnight at 4°C. The next day, sections were rinsed with PBS, blocked again before
605 incubating in secondary Alexa Fluor 488 conjugated anti-mouse antibody (1:1000, Invitrogen)
606 for 2 hours at RT. Sections were counterstained with DAPI (1:1000, Life Technologies),
607 mounted, and stored at 4°C until image analysis. mFISH images were captured on a Leica SP8
608 confocal microscope and processed using ImageJ.
609
610
611 ## Serial block-face scanning electron microscopy (SBEM)
612
613 ### Sample preparation for SBEM
614
615 One RTN4RL2$^{+/+}$ and two RTN4RL2$^{-/-}$ female mice at p36 were used for the SBEM experiments.
616 Cochleae were processed for SBEM imaging as previously described (Hua et al., 2021).
617 In brief, the animals were decapitated after CO_2 inhalation under anesthesia. The cochleae
618 were dissected from the skulls and immediately fixed by perfusing with ice-cold fixative
619 through the round and oval windows at constant flow speed using an infusion pump (Micro4,
620 WPI). The fixative solution was freshly prepared and made of 4% paraformaldehyde (Sigma-
621 Aldrich), 2.5% glutaraldehyde (Sigma-Aldrich), and 0.08 M cacodylate (pH 7.4, Sigma-Aldrich).
622 After being immersed in the fixative at 4°C for 5 hours, the cochleae were transferred to a

decalcifying solution containing the same fixative and 5% ethylenediaminetetraacetic acid (EDTA, Serva) and incubated at 4°C for 5 hours. The samples were then washed twice with 0.15 M cacodylate (pH 7.4) for 30 min each, sequentially immersed in 2% OsO_4 (Sigma-Aldrich), 2.5% ferrocyanide (Sigma-Aldrich), and again 2% OsO_4 at RT for 2, 2, and 1.5 hours. After being washed in 0.15 M cacodylate and distilled water (Sartorius) for 30 min each, the samples were sequentially incubated in filtered 1% thiocarbohydrazide (TCH, Sigma-Aldrich) solution and 2% OsO_4 at RT for 1 and 2 hours, as well as in lead aspartate solution (0.03 M, pH 5.0, adjusted with KOH) at 50 °C for 2 hours with immediate two washing steps with distilled water at RT for 30 min each. For embedding, the samples were dehydrated through graded pre-cooled acetone (Carl Roth) series (50%, 75%, 90%, for 30 min each, all cooled at 4 °C) and then pure acetone at RT (three times for 30 min each). The sample infiltration started with 1:1 and 1:2 mixtures of acetone and Spurr's resin monomer (4.1 g ERL 4221, 0.95 g DER 736, 5.9 g NSA and 1% DMAE; Sigma-Aldrich) at RT for 6 and 12 hours on a rotator. After being impregnated in pure resin for 12 hours, the samples were placed in embedding molds (Polyscience) and hardened in a pre-warmed oven at 70°C for 72 hours.

Sample trimming and SBEM imaging

The sample blocks were mounted upright along the conical center axis on aluminum metal rivets (3VMRS12, Gatan, UK) and trimmed coronally towards the modiolus using a diamond trimmer (TRIM2, Leica, Germany). For each sample, a block face of about ~ 600 x 800 mm^2, centered at the apical segment based on the anatomical landmarks, was created using an ultramicrotome (UC7, Leica, Germany). The samples were coated with a 30 nm thick gold layer using a sputter coater (ACE600, Leica, Germany). The serial images were acquired using a field-emission scanning EM (Gemini300, Carl Zeiss, Germany) equipped with an in-chamber ultramicrotome (3ViewXP, Gatan, UK) and back-scattered electron detector (Onpoint, Gatan, UK). Focal charge compensation was set to 100 % with a high vacuum chamber pressure of 2.8 x 10^3 mbar. The following parameters were set for the SBEM imaging: 12 nm pixel size, 50 nm nominal cutting thickness, 2 keV incident beam energy, and 1.5 ms pixel dwell time.

For the RTN4RL2$^{+/+}$ dataset, 2377 consecutive slices (9000 × 15000 pixels) were collected, whereas the two RTN4RL2$^{-/-}$ datasets had 3217 slices (16000 × 10000 pixels) and 2425 slices (9000 × 15000 pixels). All datasets were aligned along the z-direction using a custom MATLAB

655 script based on cross-correlation maximum between consecutive slices (Hua et al., 2022)
656 before being uploaded to webKnossos (Boergens et al., 2017) for skeleton and volume tracing.
657
658 ### Identification and quantification of auditory afferent fibers
659
660 In our SBEM datasets of the cochlea, manual skeleton tracing was carried out on all neurites
661 that originated from three neighboring habenula perforata (HP) at the center of each dataset.
662 To search for type I afferent fibers, several morphological features were used, such as
663 myelination after entering HP, radial and unbranched fiber trajectory, contact with IHCs, as
664 well as ribbon-associated terminals (Hua et al., 2021). This resulted in 115 putative type I
665 afferent fibers and further classification was made based on the presence of presynaptic
666 ribbon, fiber branching, and contact with IHC. For an illustration purpose, a type I afferent
667 fiber bundle of one RTN4RL2$^{-/-}$ dataset was volume traced and 3D rendered using Amira
668 software (Thermo Scientific, US).
669
670 ### Ribbon size measurement and synapse counting
671
672 Ribbon-type synapses were manually annotated in 18 intact IHCs captured by SBEM using
673 webKnossos. The dense core region of individual ribbon synapses was manually contoured,
674 and the associated voxels were counted for ribbon volume measurement. In the case of multi-
675 ribbon synapses, all ribbon bodies at a single active zone were summed up to yield the ribbon
676 volume.
677 ### Auditory brainstem responses
678
679 Auditory brainstem resposes (ABR) were recorded in 2- to 4-month-old mice of either sex, as
680 described previously (Luque et al., 2021). Briefly, we used a custom-made system in an
681 anechoic chamber in a calibrated open-field configuration. ABRs were recorded via needle
682 electrodes in response to tone bursts of 4, 8, 16, and 32 kHz or a click wide spectrum (2-45,2
683 KHz, 2 KHz steps) as stimuli. Tone pips of 3 ms duration (1 ms rise and fall time) were presented
684 at a rate of 60/s with alternating phases. Starting with 0 dB, the stimuli were increased in 5 dB
685 steps up to 120 dB. Hearing thresholds were determined as the minimum stimulation level
686 that produced a clearly recognizable potential. Both ears were tested. Since there was no
687 significant difference between the right and left ears, we did not consider this factor further.
688 Recordings were evaluated by three independent researchers in a blinded manner.

Data analysis and statistics

The data were analyzed using Igor Pro (Wavemetrics), Python and GraphPad Prism (GraphPad Software Inc.) software. For 2 sample comparisons, data were tested for normality and equality of variances using Jarque-Bera and F-test, respectively. Afterwards, two-tailed Student's t-test or Mann-Whitney-Wilcoxon test were performed. The latter was used when normality and/or equality of variances were not met. P-values were corrected for multiple comparisons using Holm-Šídák method. For ABR thresholds Kruskal-Wallis test followed by Dunn's multiple comparison test was used. Data is presented as mean ± standard error of the mean (SEM), unless otherwise stated. Mean, SEM and standard deviation (SD) are indicated in the figure legends as mean ± SEM, SD. Significances are reported as *$p < 0.05$, **$p < 0.01$, ***$p < 0.001$. The number of the animals is indicated as N.

Acknowledgements

We thank Sina Langer, Christiane Senger-Freitag, Sandra Gerke for expert technical support. We thank Prof. Dr. Carolin Wichmann, Dr. Susann Michanski, Julius Bahr and Sophia Mutschall for the help with the SBEM sample preparation. We thank Dr. Yi Jiang and Haoyu Wang for the visualization of neurite reconstruction. We further thank Dr. Mark Rutherford for providing tips for GluA4 immunolabeling. We would also like to thank Prof. Dr. Olaf Jahn and Lars van Werven for the TAMRA-conjugated Ctbp2 binding peptide synthesis. The study was supported by German Research Foundation through the Cluster of Excellence (EXC2067) Multiscale Bioimaging (TM) and the Leibniz Program (MO896/5 to TM) as well as by the European Research Council through the Advanced Grant "DynaHear" to TM under the European Union's Horizon 2020 Research and Innovation program (grant agreement No. 101054467), and by Fondation Pour l'Audition (FPA RD-2020-10), by the SPIN-FWF grant to CB, and by the National Natural Science Foundation of China (82171133 to YH), Industrial Support Fund of Huangpu District .in Shanghai (XK2019011 to YH), Innovative Research Team of High-level Local Universities in Shanghai (SHSMU-ZLCX20211700). NK is a member of the Hertha Sponer College from the Cluster of Excellence Multiscale Bioimaging (MBExC). TM is a Max-Planck

Fellow at the Max Planck Institute for Multidisciplinary Sciences. Open access funding provided by Max Planck Society.

Author contributions

CB, TM, YH, and NK designed the research. NK, MÜ, YQ, NB, FH, LJC, FW, ML, RG performed experiments and analyzed data. NK and TM wrote the paper with contributions of YH, CB, YQ, NB. CB, TM, YH acquired funding. All authors have reviewed and approved the final version of the manuscript for submission.

References

Appler, J. M., and Goodrich, L. V. (2011). Connecting the ear to the brain: Molecular mechanisms of auditory circuit assembly. *Prog. Neurobiol.* 93, 488–508. doi: 10.1016/j.pneurobio.2011.01.004

Bäumer, B. E., Kurz, A., Borrie, S. C., Sickinger, S., Dours-Zimmermann, M. T., Zimmermann, D. R., et al. (2014). Nogo receptor homolog NgR2 expressed in sensory DRG neurons controls epidermal innervation by interaction with Versican. *J. Neurosci. Off. J. Soc. Neurosci.* 34, 1633–1646. doi: 10.1523/JNEUROSCI.3094-13.2014

Boergens, K. M., Berning, M., Bocklisch, T., Bräunlein, D., Drawitsch, F., Frohnhofen, J., et al. (2017). webKnossos: efficient online 3D data annotation for connectomics. *Nat. Methods* 14, 691–694. doi: 10.1038/nmeth.4331

Borrie, S. C., Sartori, S. B., Lehmann, J., Sah, A., Singewald, N., and Bandtlow, C. E. (2014). Loss of Nogo receptor homolog NgR2 alters spine morphology of CA1 neurons and emotionality in adult mice. *Front. Behav. Neurosci.* 8. Available at: https://www.frontiersin.org/articles/10.3389/fnbeh.2014.00175 (Accessed March 1, 2024).

Bulankina, A. V., and Moser, T. (2012). Neural circuit development in the mammalian cochlea. *Physiology* 27, 100–112. doi: 10.1152/physiol.00036.2011

Cantu-Guerra, H. L., Papazian, M. R., Gorsky, A. L., Alekos, N. S., Caccavano, A., Karagulyan, N., et al. (2023). Cochlear hair cell innervation is dependent on a modulatory function of SEMAPHORIN-3A. *Dev. Dyn.* 252, 124–144. doi: 10.1002/dvdy.548

Carlton, A. J., Jeng, J.-Y., Grandi, F. C., De Faveri, F., Amariutei, A. E., De Tomasi, L., et al. (2024). BAI1 localizes AMPA receptors at the cochlear afferent post-synaptic density and is essential for hearing. *Cell Rep.* 43, 114025. doi: 10.1016/j.celrep.2024.114025

Coate, T. M., Scott, M. K., and Gurjar, M. (2019). Current concepts in cochlear ribbon synapse formation. *Synapse* 73, e22087. doi: 10.1002/syn.22087

Coate, T. M., Spita, N. A., Zhang, K. D., Isgrig, K. T., and Kelley, M. W. (2015). Neuropilin-2/Semaphorin-3F-mediated repulsion promotes inner hair cell innervation by spiral ganglion neurons. *eLife* 4. doi: 10.7554/eLife.07830

Defourny, J., Poirrier, A.-L., Lallemend, F., Mateo Sánchez, S., Neef, J., Vanderhaeghen, P., et al. (2013). Ephrin-A5/EphA4 signalling controls specific afferent targeting to cochlear hair cells. *Nat. Commun.* 4, 1438. doi: 10.1038/ncomms2445

Domeniconi, M., Cao, Z., Spencer, T., Sivasankaran, R., Wang, K. C., Nikulina, E., et al. (2002). Myelin-Associated Glycoprotein Interacts with the Nogo66 Receptor to Inhibit Neurite Outgrowth. *Neuron* 35, 283–290. doi: 10.1016/S0896-6273(02)00770-5

Elkon, R., Milon, B., Morrison, L., Shah, M., Vijayakumar, S., Racherla, M., et al. (2015). RFX transcription factors are essential for hearing in mice. *Nat. Commun.* 6, 8549. doi: 10.1038/ncomms9549

Fell, B., Eckrich, Stephanie, Hecker, Dietmar, Obermair, Gerald J., Flockerzi, V., Schick, B., et al. (2015). α2δ2 Controls the Function and Transsynaptic Coupling of Cav1.3 Channels in Mouse Inner Hair Cells and is Essential for Normal Hearing. *ARO Midwintermeeting*.

Fournier, A. E., GrandPre, T., and Strittmatter, S. M. (2001). Identification of a receptor mediating Nogo-66 inhibition of axonal regeneration. *Nature* 409, 341–346. doi: 10.1038/35053072

Hua, Y., Ding, X., Wang, H., Wang, F., Lu, Y., Neef, J., et al. (2021). Electron Microscopic Reconstruction of Neural Circuitry in the Cochlea. *Cell Rep.* 34, 108551. doi: 10.1016/j.celrep.2020.108551

Hua, Y., Loomba, S., Pawlak, V., Voit, K.-M., Laserstein, P., Boergens, K. M., et al. (2022). Connectomic analysis of thalamus-driven disinhibition in cortical layer 4. *Cell Rep.* 41, 111476. doi: 10.1016/j.celrep.2022.111476

Jaime Tobón, L. M., and Moser, T. (2023a). Bridging the gap between presynaptic hair cell function and neural sound encoding. doi: 10.7554/eLife.93749.1

Jaime Tobón, L. M., and Moser, T. (2023b). Ca2+ regulation of glutamate release from inner hair cells of hearing mice. *Proc. Natl. Acad. Sci.* 120, e2311539120. doi: 10.1073/pnas.2311539120

Jean, P., Morena, D. L. de la, Michanski, S., Tobón, L. M. J., Chakrabarti, R., Picher, M. M., et al. (2018). The synaptic ribbon is critical for sound encoding at high rates and with temporal precision. *eLife* 7, e29275. doi: 10.7554/eLife.29275

Jean, P., Wong Jun Tai, F., Singh-Estivalet, A., Lelli, A., Scandola, C., Megharba, S., et al. (2023). Single-cell transcriptomic profiling of the mouse cochlea: An atlas for targeted therapies. *Proc. Natl. Acad. Sci.* 120, e2221744120. doi: 10.1073/pnas.2221744120

Johnson, S. L., Safieddine, S., Mustapha, M., and Marcotti, W. (2019). Hair Cell Afferent Synapses: Function and Dysfunction. *Cold Spring Harb. Perspect. Med.* 9. doi: 10.1101/cshperspect.a033175

Jukic, A., Lei, Z., Cebul, E. R., Pinter, K., Tadesse, Y., Jarysta, A., et al. (2024). Presynaptic Nrxn3 is essential for ribbon-synapse maturation in hair cells. *Development* 151, dev202723. doi: 10.1242/dev.202723

Jung, J. S., Zhang, K. D., Wang, Z., McMurray, M., Tkaczuk, A., Ogawa, Y., et al. (2019). Semaphorin-5B Controls Spiral Ganglion Neuron Branch Refinement during Development. *J. Neurosci.* 39, 6425–6438. doi: 10.1523/JNEUROSCI.0113-19.2019

Karagulyan, N., Thirumalai, A., Michanski, S., Qi, Y., Fang, Q., Wang, H., et al. (2025). Gating of hair cell Ca2+ channels governs the activity of cochlear neurons. 2025.01.23.634330. doi: 10.1101/2025.01.23.634330

Koundakjian, E. J., Appler, J. L., and Goodrich, L. V. (2007). Auditory neurons make stereotyped wiring decisions before maturation of their targets. *J. Neurosci. Off. J. Soc. Neurosci.* 27, 14078–14088. doi: 10.1523/JNEUROSCI.3765-07.2007

Kujawa, S. G., and Liberman, M. C. (2009). Adding insult to injury: cochlear nerve degeneration after “temporary” noise-induced hearing loss. *J. Neurosci.* 29, 14077.

Kujawa, S. G., and Liberman, M. C. (2015). Synaptopathy in the noise-exposed and aging cochlea: Primary neural degeneration in acquired sensorineural hearing loss. *Hear. Res.* 330, 191–199. doi: 10.1016/j.heares.2015.02.009

Kwiatkowska, M., Reinhard, J., Roll, L., Kraft, N., Dazert, S., Faissner, A., et al. (2016). The expression pattern and inhibitory influence of Tenascin-C on the growth of spiral ganglion neurons suggest a regulatory role as boundary formation molecule in the postnatal mouse inner ear. *Neuroscience* 319, 46–58. doi: 10.1016/j.neuroscience.2016.01.039

Liberman, L. D., and Liberman, M. C. (2016). Postnatal maturation of auditory-nerve heterogeneity, as seen in spatial gradients of synapse morphology in the inner hair cell area. *Hear. Res.* 339, 12–22. doi: 10.1016/j.heares.2016.06.002

Lindau, M., and Neher, E. (1988). Patch-clamp techniques for time-resolved capacitance measurements in single cells. *Pflüg. Arch. Eur. J. Physiol.* 411, 137–146.

Liu, H., Chen, L., Giffen, K. P., Stringham, S. T., Li, Y., Judge, P. D., et al. (2018). Cell-Specific Transcriptome Analysis Shows That Adult Pillar and Deiters’ Cells Express Genes Encoding Machinery for Specializations of Cochlear Hair Cells. *Front. Mol. Neurosci.* 11. doi: 10.3389/fnmol.2018.00356

Lu, Y., Liu, J., Li, B., Wang, H., Wang, F., Wang, S., et al. (2024). Spatial patterns of noise-induced inner hair cell ribbon loss in the mouse mid-cochlea. *iScience* 27, 108825. doi: 10.1016/j.isci.2024.108825

Luque, M., Schrott-Fischer, A., Dudas, J., Pechriggl, E., Brenner, E., Rask-Andersen, H., et al. (2021). HCN channels in the mammalian cochlea: Expression pattern, subcellular location, and age-dependent changes. *J. Neurosci. Res.* 99, 699–728. doi: 10.1002/jnr.24754

Matsubara, A., Laake, J. H., Davanger, S., Usami, S., and Ottersen, O. P. (1996). Organization of AMPA receptor subunits at a glutamate synapse: a quantitative immunogold analysis of hair cell synapses in the rat organ of Corti. *J. Neurosci.* 16, 4457.

Meyer, A. C., and Moser, T. (2010). Structure and function of cochlear afferent innervation. *Curr. Opin. Otolaryngol. Head Neck Surg.* 18, 441–446. doi: 10.1097/MOO.0b013e32833e0586

Michanski, S., Smaluch, K., Steyer, A. M., Chakrabarti, R., Setz, C., Oestreicher, D., et al. (2019). Mapping developmental maturation of inner hair cell ribbon synapses in the apical mouse cochlea. *Proc. Natl. Acad. Sci.* 116, 6415–6424. doi: 10.1073/pnas.1812029116

Mironova, Y. A., and Giger, R. J. (2013). Where no synapses go: gatekeepers of circuit remodeling and synaptic strength. *Trends Neurosci.* 36, 363–373. doi: 10.1016/j.tins.2013.04.003

Moser, T., and Beutner, D. (2000). Kinetics of exocytosis and endocytosis at the cochlear inner hair cell afferent synapse of the mouse. *Proc. Natl. Acad. Sci.* 97, 883–888. doi: 10.1073/pnas.97.2.883

Moverman, D. J., Liberman, L. D., Kraemer, S., Corfas, G., and Liberman, M. C. (2023). Ultrastructure of noise-induced cochlear synaptopathy. *Sci. Rep.* 13, 19456. doi: 10.1038/s41598-023-46859-6

Niedzielski, A. S., and Wenthold, R. J. (1995). Expression of AMPA, kainate, and NMDA receptor subunits in cochlear and vestibular ganglia. *J. Neurosci.* 15, 2338.

Ohn, T.-L., Rutherford, M. A., Jing, Z., Jung, S., Duque-Afonso, C. J., Hoch, G., et al. (2016). Hair cells use active zones with different voltage dependence of Ca^{2+} influx to decompose sounds into complementary neural codes. *Proc. Natl. Acad. Sci.* 113, E4716–E4725. doi: 10.1073/pnas.1605737113

Özçete, Ö. D., and Moser, T. (2021). A sensory cell diversifies its output by varying Ca^{2+} influx-release coupling among active zones. *EMBO J.* 40, e106010. doi: 10.15252/embj.2020106010

Ramirez, M. A., Ninoyu, Y., Miller, C., Andrade, L. R., Edassery, S., Bomba-Warczak, E., et al. (2022). Cochlear ribbon synapse maturation requires Nlgn1 and Nlgn3. *iScience* 25, 104803. doi: 10.1016/j.isci.2022.104803

Roux, I., Safieddine, S., Nouvian, R., Grati, M., Simmler, M.-C., Bahloul, A., et al. (2006). Otoferlin, Defective in a Human Deafness Form, Is Essential for Exocytosis at the Auditory Ribbon Synapse. *Cell* 127, 277–289. doi: 10.1016/j.cell.2006.08.040

Ruel, J., Emery, S., Nouvian, R., Bersot, T., Amilhon, B., Van Rybroek, J. M., et al. (2008). Impairment of SLC17A8 Encoding Vesicular Glutamate Transporter-3, VGLUT3, Underlies Nonsyndromic Deafness DFNA25 and Inner Hair Cell Dysfunction in Null Mice. *Am. J. Hum. Genet.* 83, 278–292. doi: 10.1016/j.ajhg.2008.07.008

Rutherford, M. A., Bhattacharyya, A., Xiao, M., Cai, H.-M., Pal, I., and Rubio, M. E. (2023). GluA3 subunits are required for appropriate assembly of AMPAR GluA2 and GluA4 subunits on cochlear afferent synapses and for presynaptic ribbon modiolar-pillar morphology. *eLife* 12, e80950. doi: 10.7554/eLife.80950

Schwab, M. E. (2010). Functions of Nogo proteins and their receptors in the nervous system. *Nat. Rev. Neurosci.* 11, 799–811. doi: 10.1038/nrn2936

879 Seal, R. P., Akil, O., Yi, E., Weber, C. M., Grant, L., Yoo, J., et al. (2008). Sensorineural Deafness
880 and Seizures in Mice Lacking Vesicular Glutamate Transporter 3. *Neuron* 57, 263–275.
881 doi: 10.1016/j.neuron.2007.11.032

882 Sherrill, H. E., Jean, P., Driver, E. C., Sanders, T. R., Fitzgerald, T. S., Moser, T., et al. (2019).
883 Pou4f1 Defines a Subgroup of Type I Spiral Ganglion Neurons and Is Necessary for
884 Normal Inner Hair Cell Presynaptic Ca2+ Signaling. *J. Neurosci.* 39, 5284–5298. doi:
885 10.1523/JNEUROSCI.2728-18.2019

886 Shrestha, B. R., Chia, C., Wu, L., Kujawa, S. G., Liberman, M. C., and Goodrich, L. V. (2018).
887 Sensory Neuron Diversity in the Inner Ear Is Shaped by Activity. *Cell* 174, 1229-
888 1246.e17. doi: 10.1016/j.cell.2018.07.007

889 Shrestha, B. R., Wu, L., and Goodrich, L. V. (2023). Runx1 controls auditory sensory neuron
890 diversity in mice. *Dev. Cell* 58, 306-319.e5. doi: 10.1016/j.devcel.2023.01.008

891 Sonntag, M., Blosa, M., Schmidt, S., Reimann, K., Blum, K., Eckrich, T., et al. (2018). Synaptic
892 coupling of inner ear sensory cells is controlled by brevican-based extracellular
893 matrix baskets resembling perineuronal nets. *BMC Biol.* 16, 99. doi: 10.1186/s12915-
894 018-0566-8

895 Stephenson, J. R., Paavola, K. J., Schaefer, S. A., Kaur, B., Van Meir, E. G., and Hall, R. A.
896 (2013). Brain-specific Angiogenesis Inhibitor-1 Signaling, Regulation, and Enrichment
897 in the Postsynaptic Density. *J. Biol. Chem.* 288, 22248–22256. doi:
898 10.1074/jbc.M113.489757

899 Vaccaro, G., Dumoulin, A., Zuñiga, N. R., Bandtlow, C. E., and Stoeckli, E. T. (2022). The Nogo-
900 66 Receptors NgR1 and NgR3 Are Required for Commissural Axon Pathfinding. *J.*
901 *Neurosci.* 42, 4087–4100. doi: 10.1523/JNEUROSCI.1390-21.2022

902 Venkatesh, K., Chivatakarn, O., Lee, H., Joshi, P. S., Kantor, D. B., Newman, B. A., et al. (2005).
903 The Nogo-66 Receptor Homolog NgR2 Is a Sialic Acid-Dependent Receptor Selective
904 for Myelin-Associated Glycoprotein. *J. Neurosci.* 25, 808–822. doi:
905 10.1523/JNEUROSCI.4464-04.2005

906 Wang, J., Miao, Y., Wicklein, R., Sun, Z., Wang, J., Jude, K. M., et al. (2021). RTN4/NoGo-
907 receptor binding to BAI adhesion-GPCRs regulates neuronal development. *Cell* 184,
908 5869-5885.e25. doi: 10.1016/j.cell.2021.10.016

909 Wang, K. C., Koprivica, V., Kim, J. A., Sivasankaran, R., Guo, Y., Neve, R. L., et al. (2002a).
910 Oligodendrocyte-myelin glycoprotein is a Nogo receptor ligand that inhibits neurite
911 outgrowth. *Nature* 417, 941–944. doi: 10.1038/nature00867

912 Wang, X., Chun, S.-J., Treloar, H., Vartanian, T., Greer, C. A., and Strittmatter, S. M. (2002b).
913 Localization of Nogo-A and Nogo-66 Receptor Proteins at Sites of Axon–Myelin and
914 Synaptic Contact. *J. Neurosci.* 22, 5505–5515. doi: 10.1523/JNEUROSCI.22-13-
915 05505.2002

Wills, Z. P., Mandel-Brehm, C., Mardinly, A. R., McCord, A. E., Giger, R. J., and Greenberg, M. E. (2012). The Nogo Receptor Family Restricts Synapse Number in the Developing Hippocampus. *Neuron* 73, 466–481. doi: 10.1016/j.neuron.2011.11.029

Wong, A. B., Rutherford, M. A., Gabrielaitis, M., Pangršič, T., Göttfert, F., Frank, T., et al. (2014). Developmental refinement of hair cell synapses tightens the coupling of Ca2+ influx to exocytosis. *EMBO J.* 33, 247–264. doi: 10.1002/embj.201387110

Wörter, V., Schweigreiter, R., Kinzel, B., Mueller, M., Barske, C., Böck, G., et al. (2009). Inhibitory activity of myelin-associated glycoprotein on sensory neurons is largely independent of NgR1 and NgR2 and resides within Ig-Like domains 4 and 5. *PloS One* 4, e5218. doi: 10.1371/journal.pone.0005218

Zenisek, D., Horst, N. K., Merrifield, C., Sterling, P., and Matthews, G. (2004). Visualizing synaptic ribbons in the living cell. *J. Neurosci. Off. J. Soc. Neurosci.* 24, 9752–9759. doi: 10.1523/JNEUROSCI.2886-04.2004

Supplementary Figures

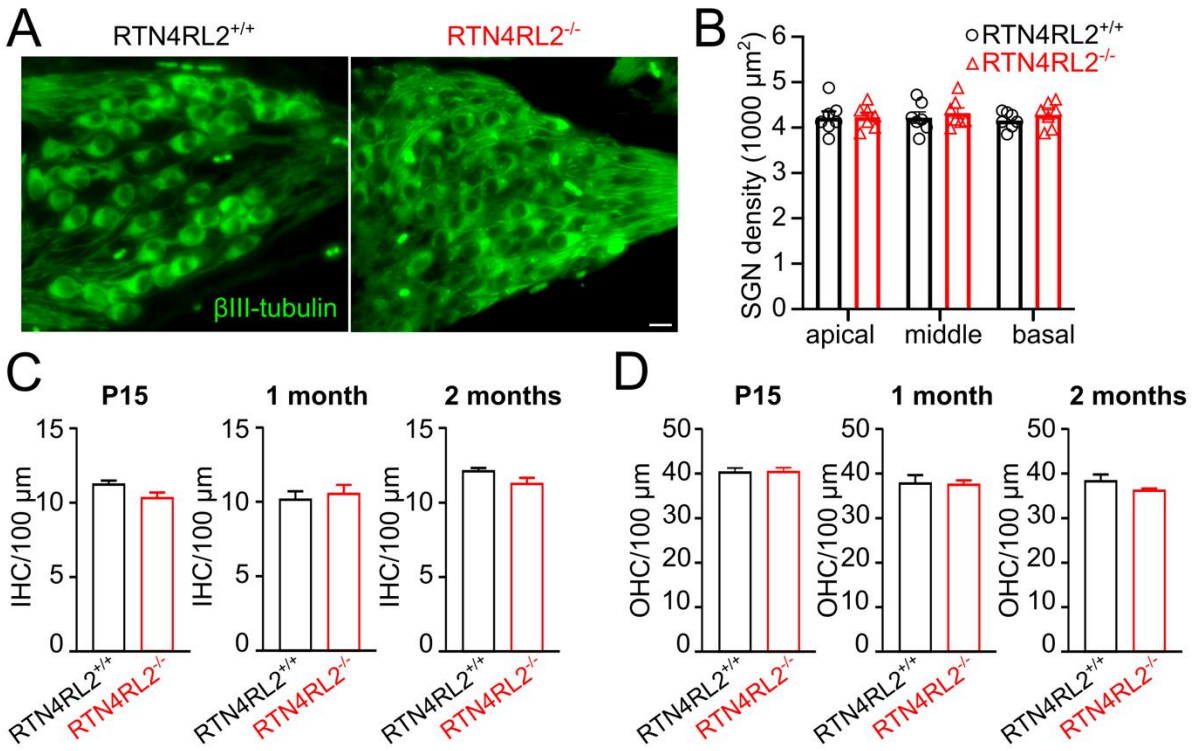

Figure 2-figure supplement 1. Cochlear cell densities are not changed in RTN4RL2$^{-/-}$ mice. (**A**) Mid/Basal-modiolar sections labeled for βIII-tubulin (green, neurons) from p40 RTN4RL2$^{+/+}$ and RTN4RL2$^{-/-}$ mice. Exemplary section for RTN4RL2$^{-/-}$ is the zoomed out image presented in figure 1C. (**B**) Quantitative analysis shows that the density of SGN cell bodies are similar between RTN4RL2$^{-/-}$ and control cochleae. Data is presented as mean ± SD; N = 7 per group. Scale bar = 10 µm. (**C, D**) IHC (C) and OHC (D) densities are not affected in P15, 1 month and 2 months old RTN4RL2$^{-/-}$ mice.

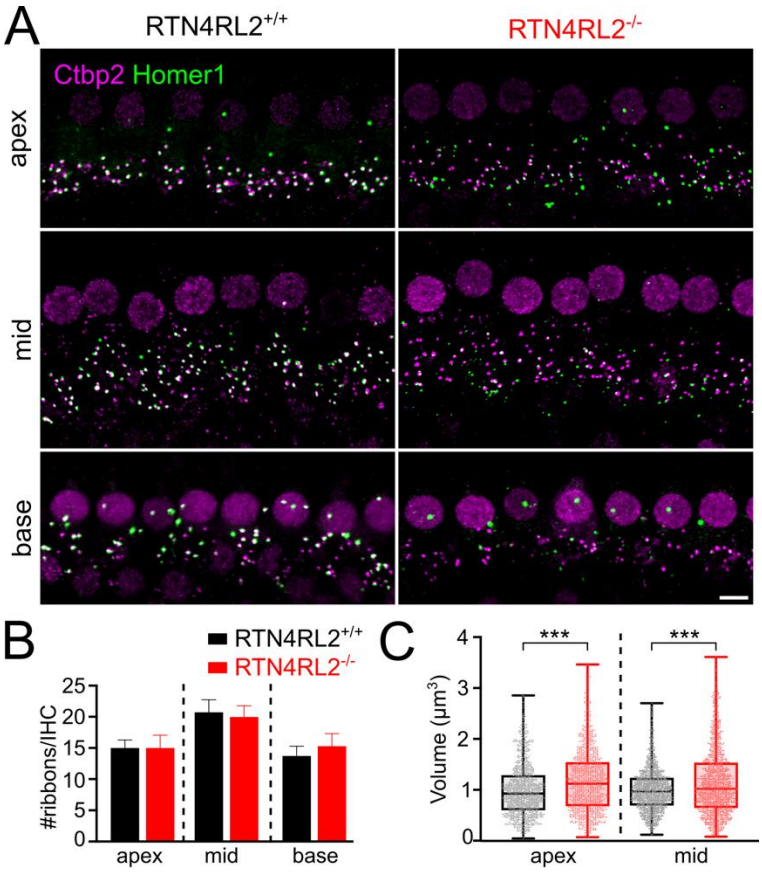

Figure 2-figure supplement 2. Intact number but enlarged size of the ribbons in RTN4RL2$^{-/-}$ IHCs. (**A**) Maximum intensity projections of representative IHCs from apical, mid and basal regions of RTN4RL2$^{+/+}$ (left) and RTN4RL2$^{-/-}$ (right) cochleae of p21-30 mice. Synapses are visualized by staining against Ctbp2/Ribeye (ribbons) and Homer1 (PSDs). Scale bar = 5 µm. (**B**) The number of the ribbons is not affected along the tonotopic axis in RTN4RL2$^{-/-}$ cochleae. (**C**) The size of the ribbons is increased in IHCs of both apical and middle turns in RTN4RL2$^{-/-}$ cochleae ($p < 0.001$, Mann-Whitney-Wilcoxon test). N = 6 animals/genotype. Box-whisker plots show the median, 25/75 percentiles (box) and the range (whiskers). Individual data points are overlaid.

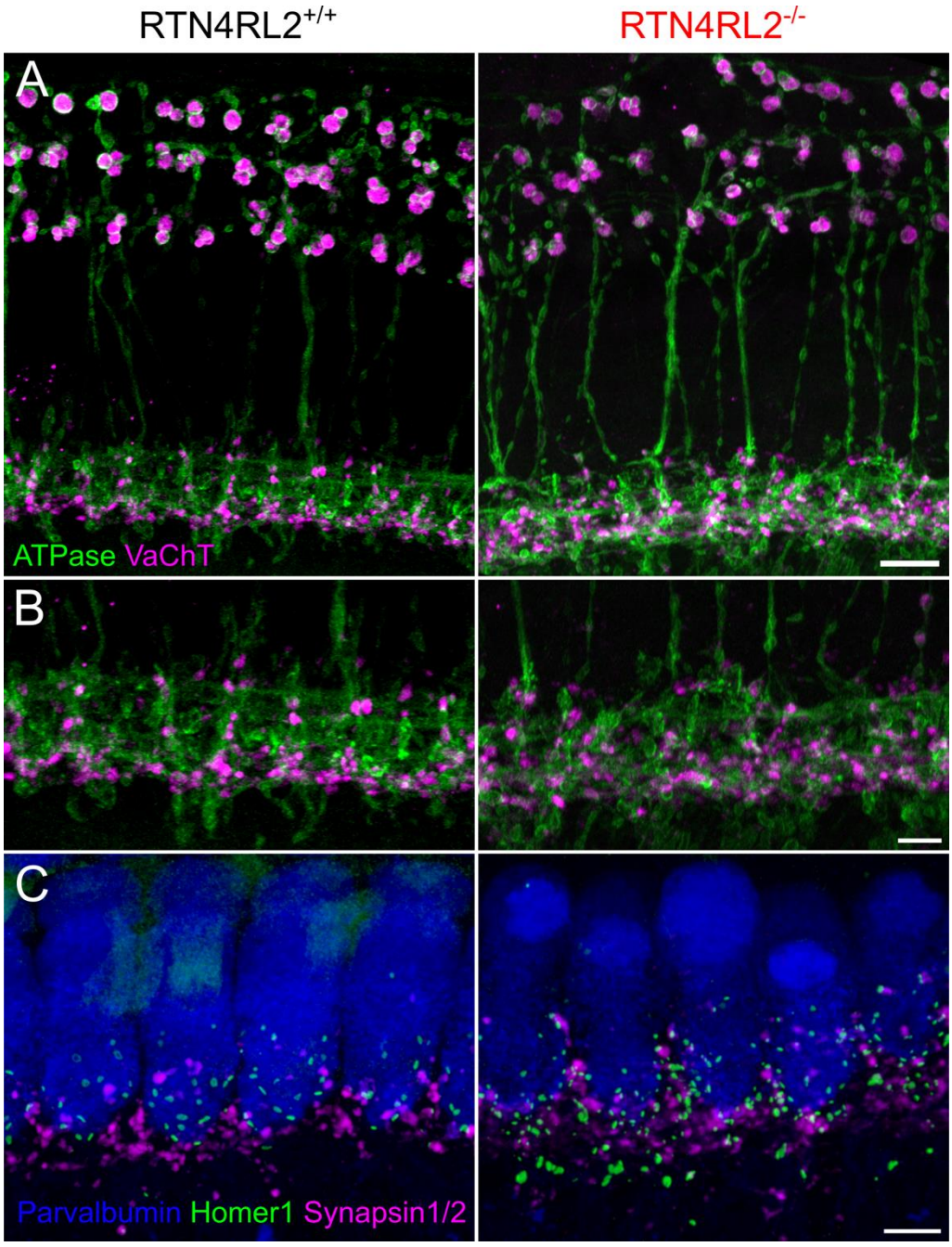

Figure 2-figure supplement 3. Efferent innervation pattern in RTN4RL2$^{-/-}$ cochleae. (**A**) Maximum intensity projections of confocal stacks of outer and inner hair cell regions at the apical region of the cochlea from p21-30 RTN4RL2$^{+/+}$ (left) and RTN4RL2$^{-/-}$ (right) mice. SGN fibers/terminals and efferent terminals are visualized staining for Na^+/K^+ ATPase and vesicular acetylcholine transporter (VaChT), respectively. Scale Bar = 10 µm (**B**) Same as (A) but zoomed into the IHC region. Scale Bar = 5 µm (**C**) Maximum intensity projections of confocal stacks of a row of apical IHC region from p21 RTN4RL2$^{+/+}$ (left) and RTN4RL2$^{-/-}$ (right) mice. Presynaptic efferent terminals were stained with an anti-synapsin1/2 antibody. Scale bar = 5 µm.

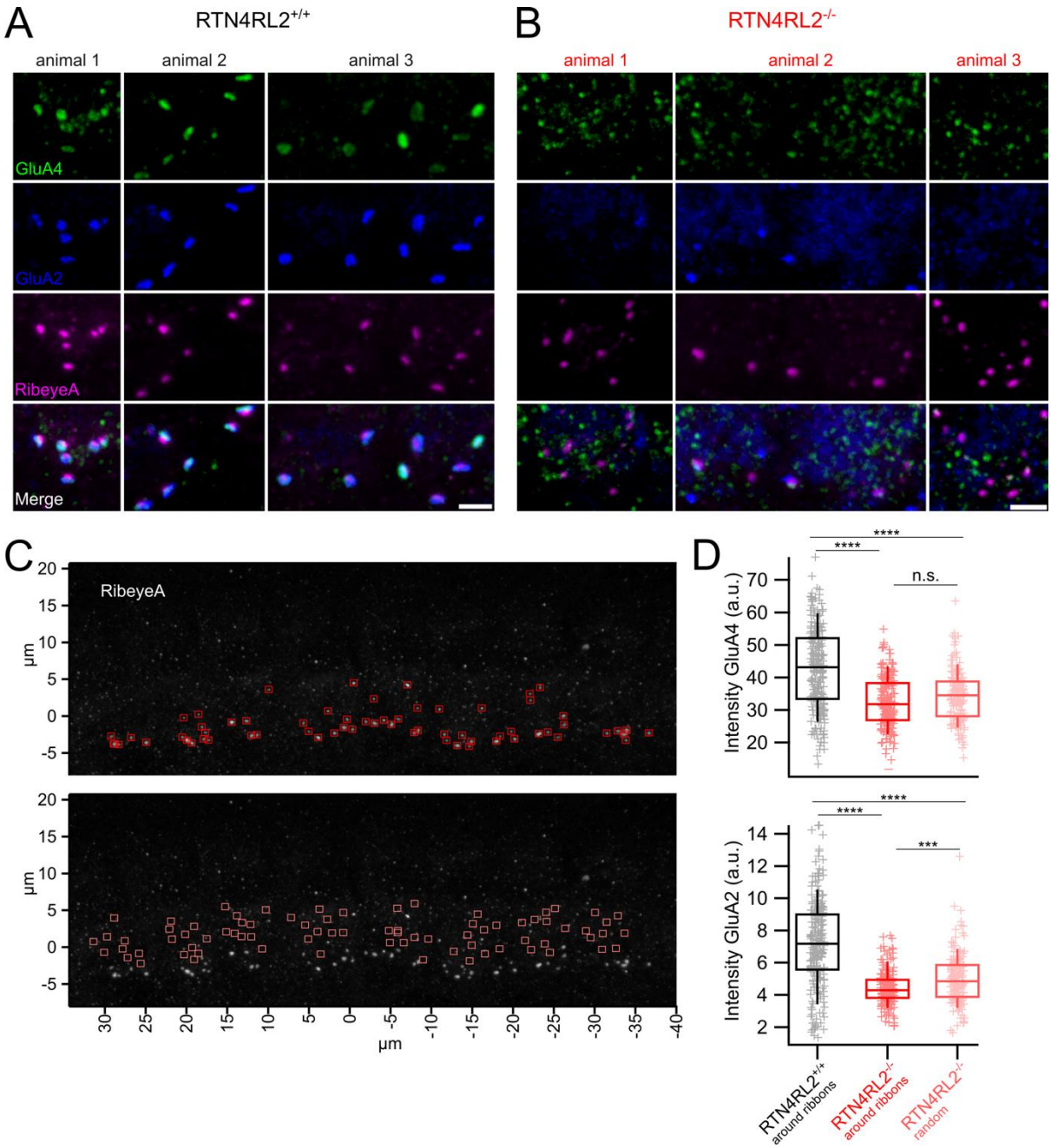

Figure 3-figure supplement 1. No apparent GluA4 signal juxtaposing presynaptic ribbons at IHC synapses of RTN4RL2$^{-/-}$ mice. (**A, B**) Maximum intensity projections of a few imaging planes from apical IHC synaptic regions of 14-week-old N = 3 RTN4RL2$^{+/+}$ (A) and N = 3 RTN4RL2$^{-/-}$ (B) mice immunostained against GluA4, GluA2 and RibeyeA. Scale bars = 2 µm. (**C**) Fluorescence intensities of GluA4 and GluA2 channels were analyzed as the sum of all pixel intensities in approximately 1×1×1 µm³ volumes around the center of mass of RibeyeA immunofluorescent puncta (red boxes, top image). Background GluA4 and GluA2 fluorescence signals were calculated in the same way but outside the ribbons, at random spots inside IHCs (pink boxes, bottom image). Images show the maximum intensity projection of the IHC region in an RTN4RL2$^{-/-}$ mouse. (**D**) Fluorescence intensities of GluA4 (top) and GluA2 (bottom) channels at ribbons of RTN4RL2$^{-/-}$ mice do not show a significant increase compared to the background (RTN4RL2$^{-/-}$ random) but are significantly decreased compared to RTN4RL2$^{+/+}$ (Mann-Whitney-Wilcoxon test followed by Bonferroni multiple-comparison correction). Box-

979 whisker plots show the median, 25/75 percentiles (box) and 10/90 percentiles (whiskers).
980 Individual data points are overlaid.
981

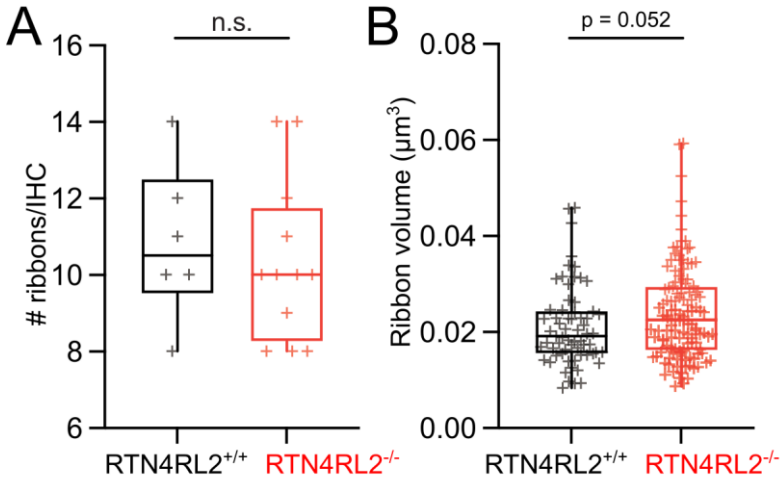

982
983
984 **Figure 4-figure supplement 1. Quantification of ribbon number and volume in SBEM**
985 **reconstructions.** (**A**) The number of ribbons is not changed in RTN4RL2$^{-/-}$ IHCs (RTN4RL2$^{-/-}$:
986 10.3 ± 0.61, SD = 2.1, n = 12, N = 2 vs. RTN4RL2$^{+/+}$: 10.8 ± 0.83, SD = 2.04, n = 6, N = 1; p = 0.54,
987 Mann-Whitney-Wilcoxon test). (**B**) Ribbon volumes tend to be larger in RTN4RL2$^{-/-}$ IHCs
988 without reaching statistical significance (RTN4RL2$^{-/-}$: 0.024 ± 0.001 µm^3, SD = 0.01 µm^3, n =
989 125 ribbons in 12 IHCs, N = 2 vs. RTN4RL2$^{+/+}$: 0.021 ± 0.001 µm^3, SD = 0.008 µm^3, n = 65 ribbons
990 in 6 IHCs, N = 1; p = 0.06, Mann-Whitney-Wilcoxon test). Box-whisker plots show the median,
991 25/75 percentiles (box) and the range (whiskers). Individual data points are overlaid.

992

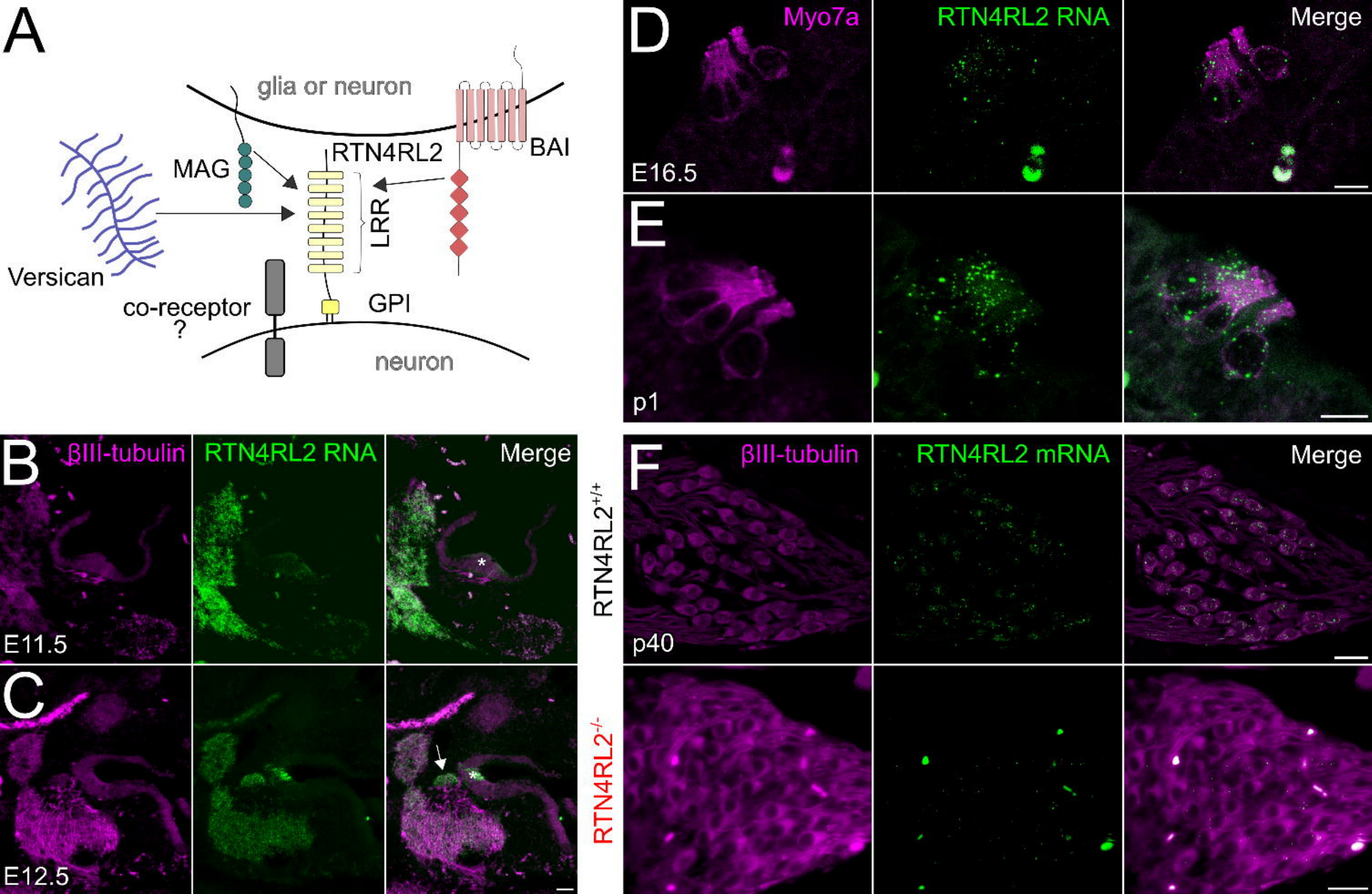
A
glia or neuron
MAG
RTN4RL2
BAI
LRR
Versican
co-receptor
?
GPI
neuron
D
Myo7a
RTN4RL2 RNA
Merge
E16.5
E
p1
B
βIII-tubulin
RTN4RL2 RNA
Merge
E11.5
C
E12.5
RTN4RL2+/+
RTN4RL2-/-
F
βIII-tubulin
RTN4RL2 mRNA
Merge
p40

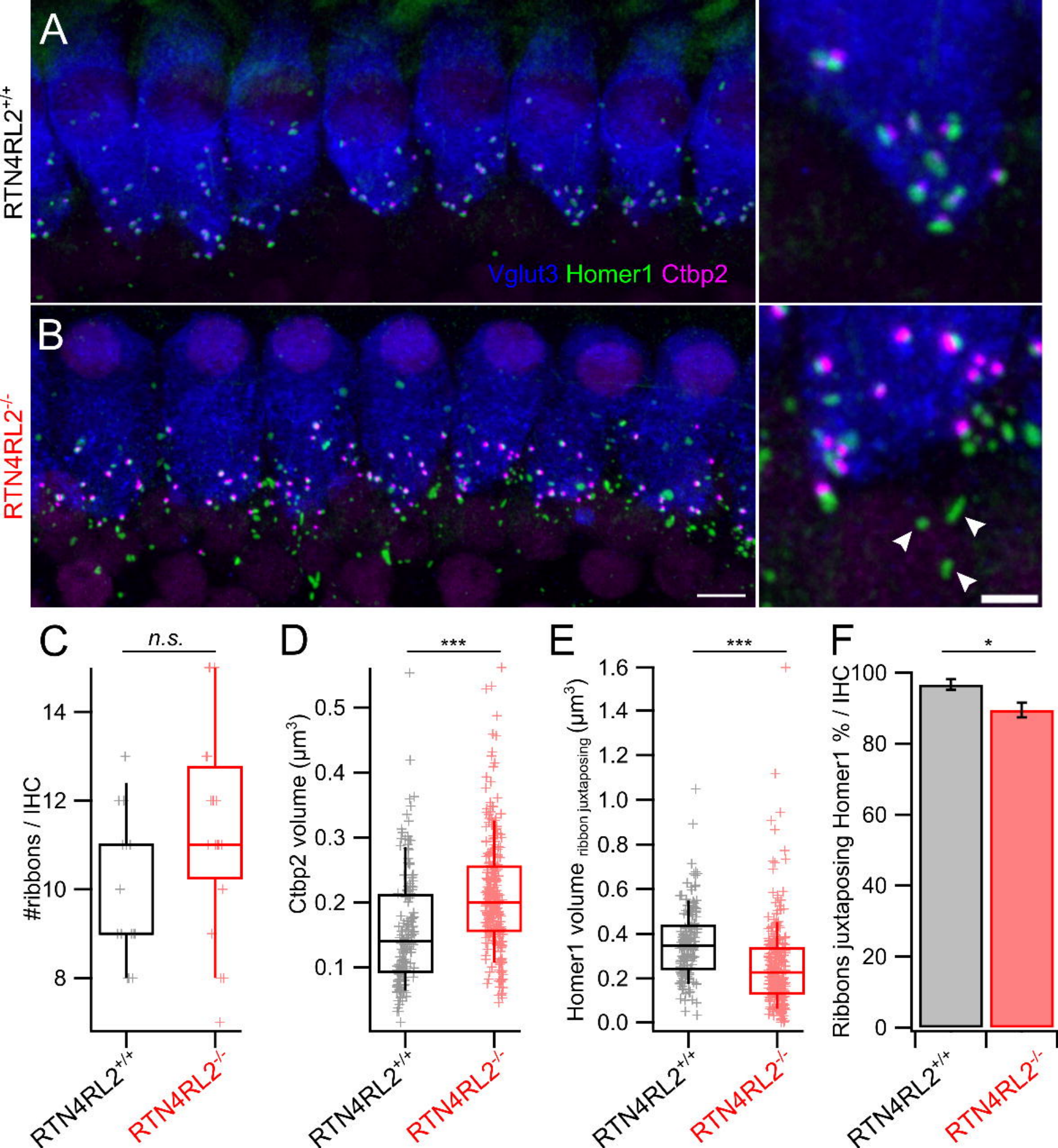
A
RTN4RL2+/+
Vglut3 Homer1 Ctbp2
B
RTN4RL2-/-
C
n.s.
#ribbons / IHC
14
12
10
8
RTN4RL2+/+
RTN4RL2-/-
D
***
Ctbp2 volume (µm3)
0.5
0.4
0.3
0.2
0.1
RTN4RL2+/+
RTN4RL2-/-
E
***
Homer1 volume ribbon juxtaposing (µm3)
1.6
1.4
1.2
1.0
0.8
0.6
0.4
0.2
0.0
RTN4RL2+/+
RTN4RL2-/-
F
*
Ribbons juxtaposing Homer1 % / IHC
100
80
60
40
20
0
RTN4RL2+/+
RTN4RL2-/-

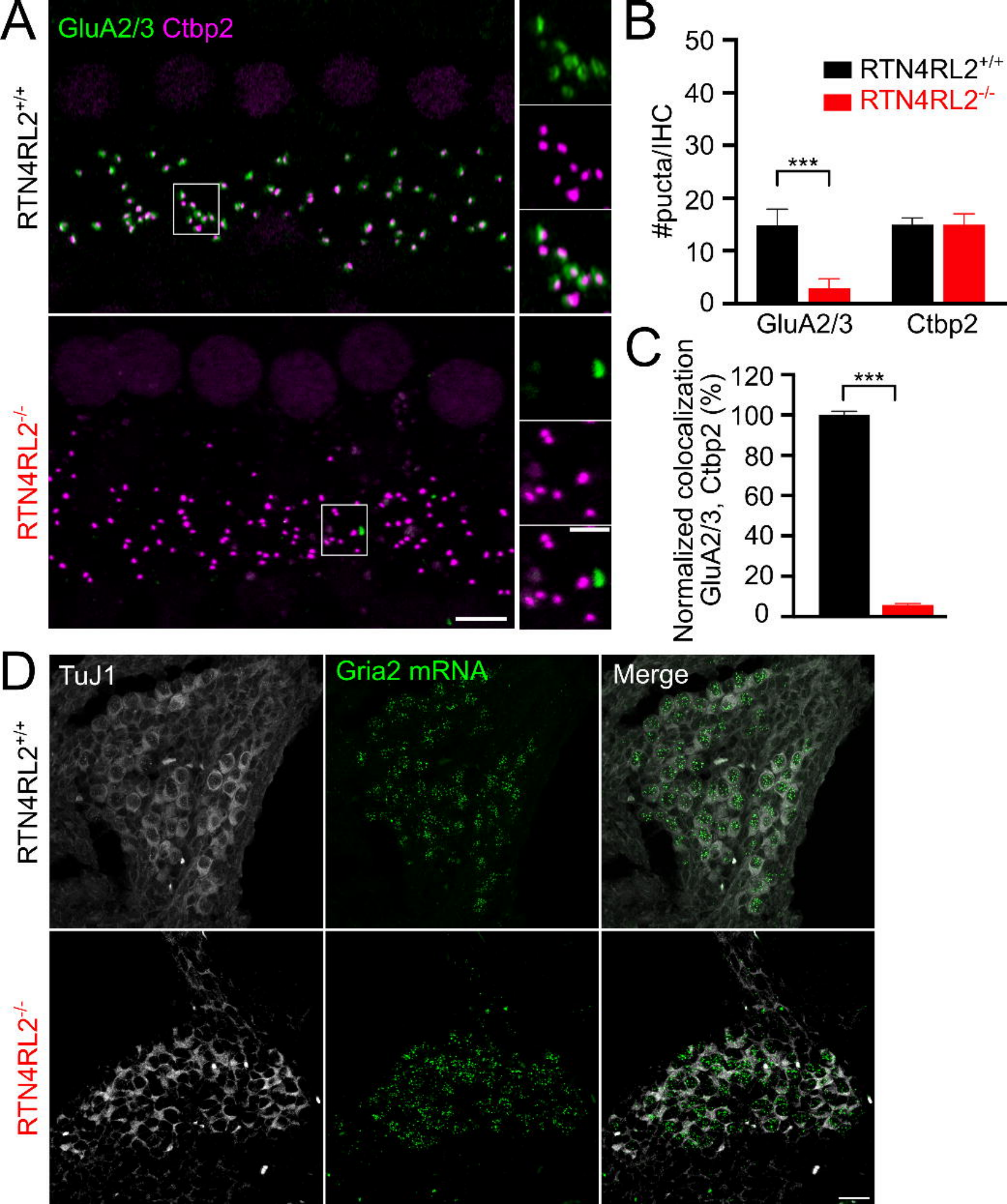
A
GluA2/3 Ctbp2
RTN4RL2+/+
RTN4RL2-/-
B
RTN4RL2+/+
RTN4RL2-/-
#pucta/IHC
50
40
30
20
10
0
***
GluA2/3
Ctbp2
C
Normalized colocalization GluA2/3, Ctbp2 (%)
120
100
80
60
40
20
0
***
D
TuJ1
Gria2 mRNA
Merge
RTN4RL2+/+
RTN4RL2-/-

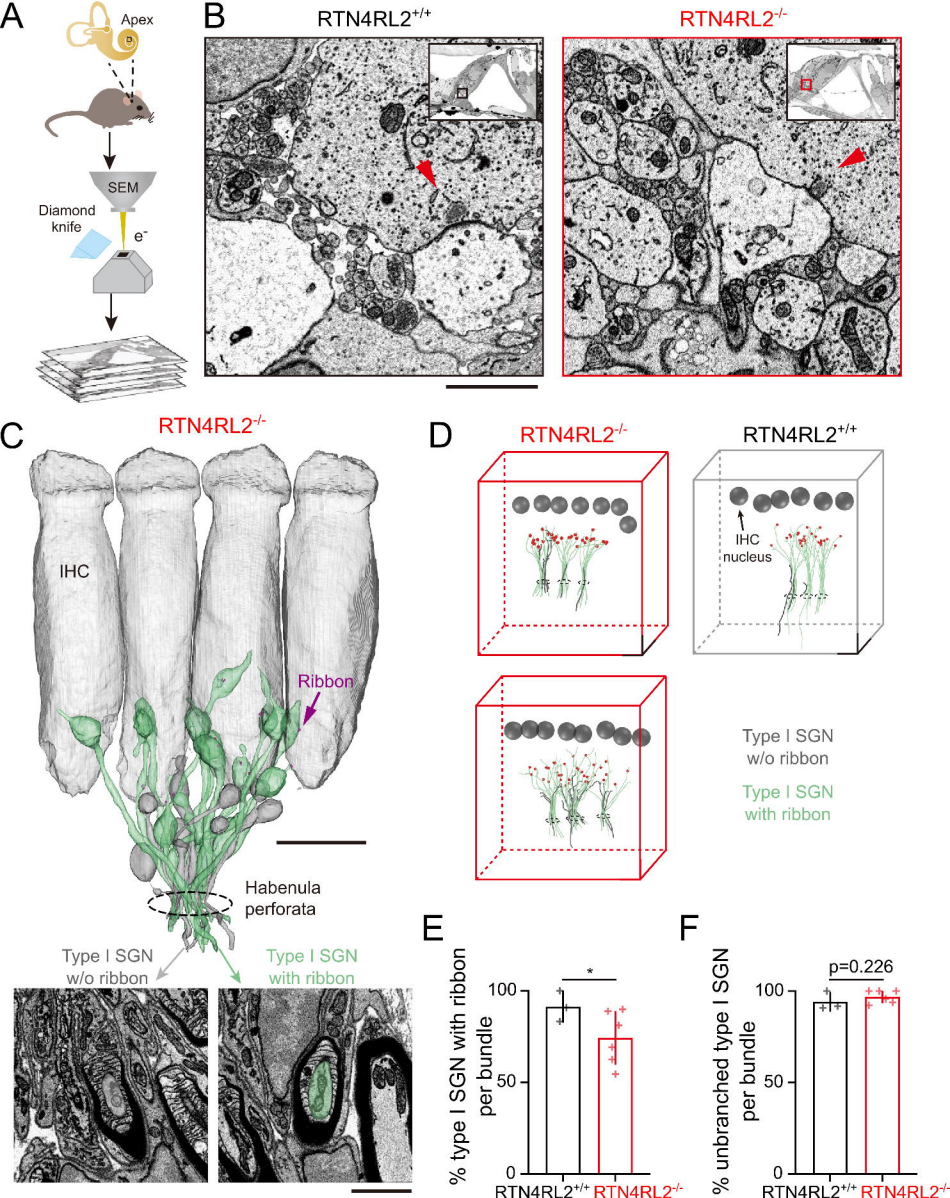
A
Apex
SEM
Diamond knife
e⁻
B
RTN4RL2+/+
RTN4RL2-/-
C
RTN4RL2-/-
IHC
Ribbon
Habenula perforata
Type I SGN w/o ribbon
Type I SGN with ribbon
D
RTN4RL2-/-
RTN4RL2+/+
IHC nucleus
Type I SGN w/o ribbon
Type I SGN with ribbon
E
% type I SGN with ribbon per bundle
100
50
0
*
RTN4RL2+/+
RTN4RL2-/-
F
% unbranched type I SGN per bundle
100
50
0
p=0.226
RTN4RL2+/+
RTN4RL2-/-

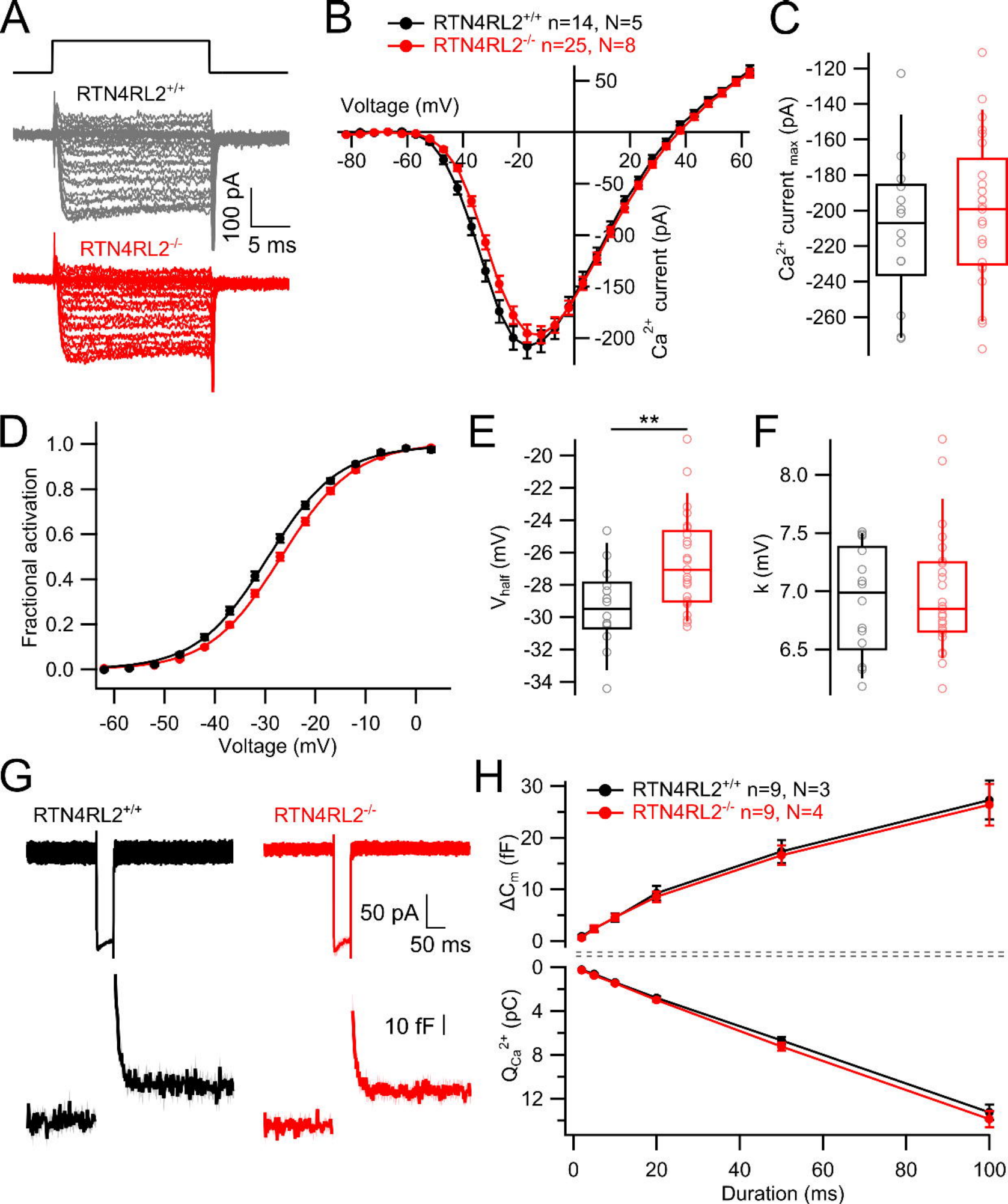
A
RTN4RL2+/+
RTN4RL2-/-
100 pA
5 ms
B
RTN4RL2+/+ n=14, N=5
RTN4RL2-/- n=25, N=8
Voltage (mV)
Ca2+ current (pA)
C
Ca2+ current max (pA)
D
Fractional activation
Voltage (mV)
E
**
Vhalf (mV)
F
k (mV)
G
RTN4RL2+/+
RTN4RL2-/-
50 pA
50 ms
10 fF
H
RTN4RL2+/+ n=9, N=3
RTN4RL2-/- n=9, N=4
ΔCm (fF)
QCa2+ (pC)
Duration (ms)

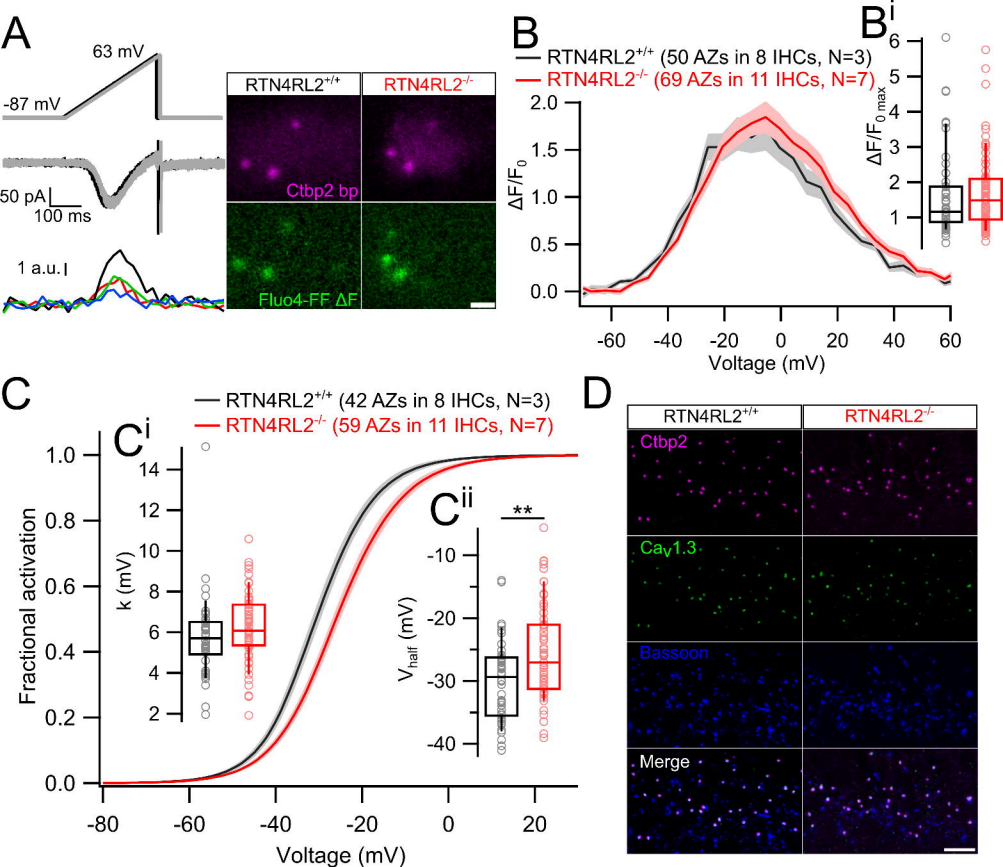
A
63 mV
-87 mV
50 pA
100 ms
1 a.u.
RTN4RL2+/+
RTN4RL2-/-
Ctbp2 bp
Fluo4-FF ΔF
B
RTN4RL2+/+ (50 AZs in 8 IHCs, N=3)
RTN4RL2-/- (69 AZs in 11 IHCs, N=7)
ΔF/F0
Voltage (mV)
Bi
ΔF/F0 max
C
RTN4RL2+/+ (42 AZs in 8 IHCs, N=3)
RTN4RL2-/- (59 AZs in 11 IHCs, N=7)
Fractional activation
Voltage (mV)
Ci
k (mV)
Cii
Vhalf (mV)
**
D
RTN4RL2+/+
RTN4RL2-/-
Ctbp2
CaV1.3
Bassoon
Merge

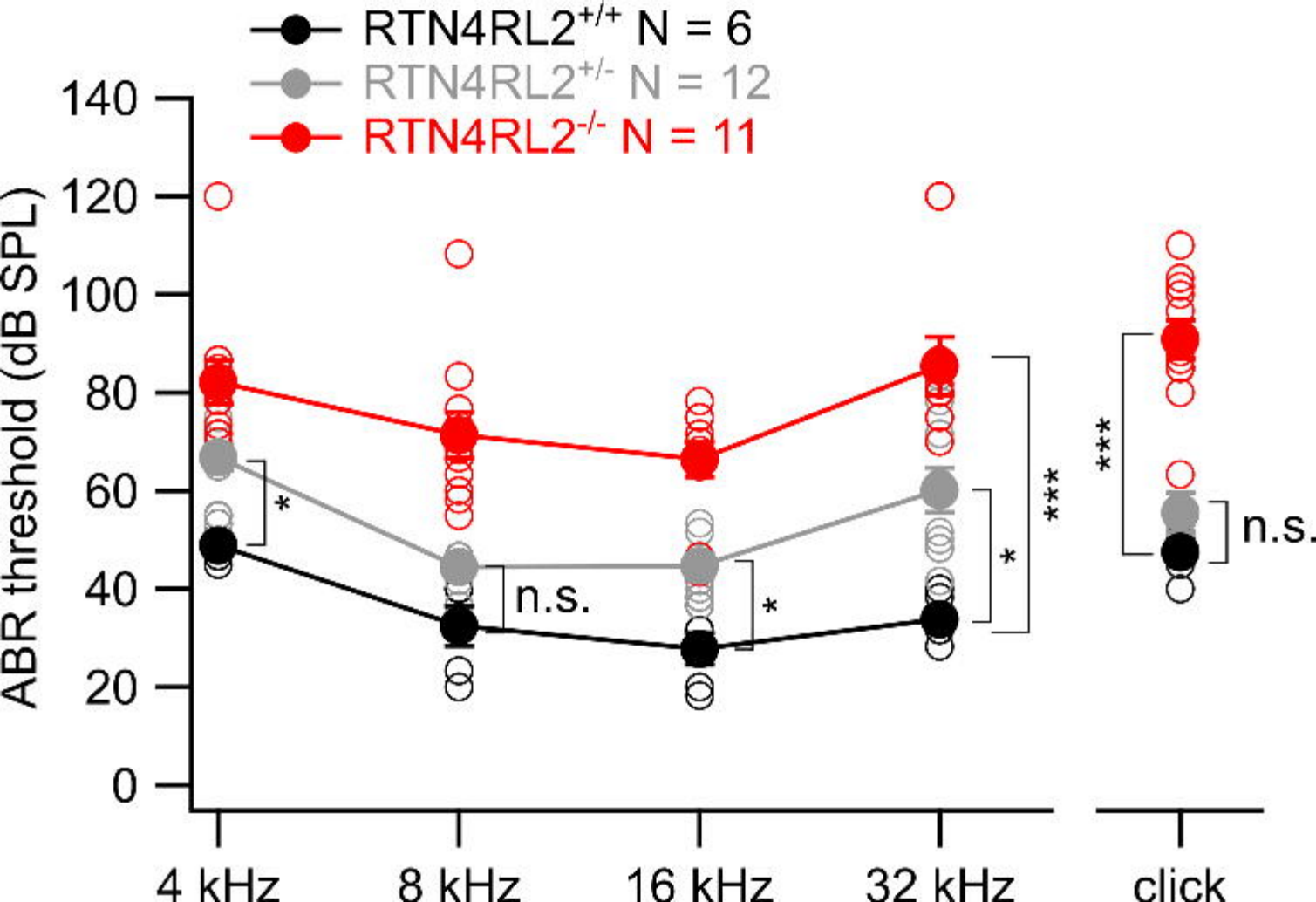
RTN4RL2+/+ N = 6
RTN4RL2+/- N = 12
RTN4RL2-/- N = 11
ABR threshold (dB SPL)
140
120
100
80
60
40
20
0
*
n.s.
*
*
***
***
n.s.
4 kHz
8 kHz
16 kHz
32 kHz
click

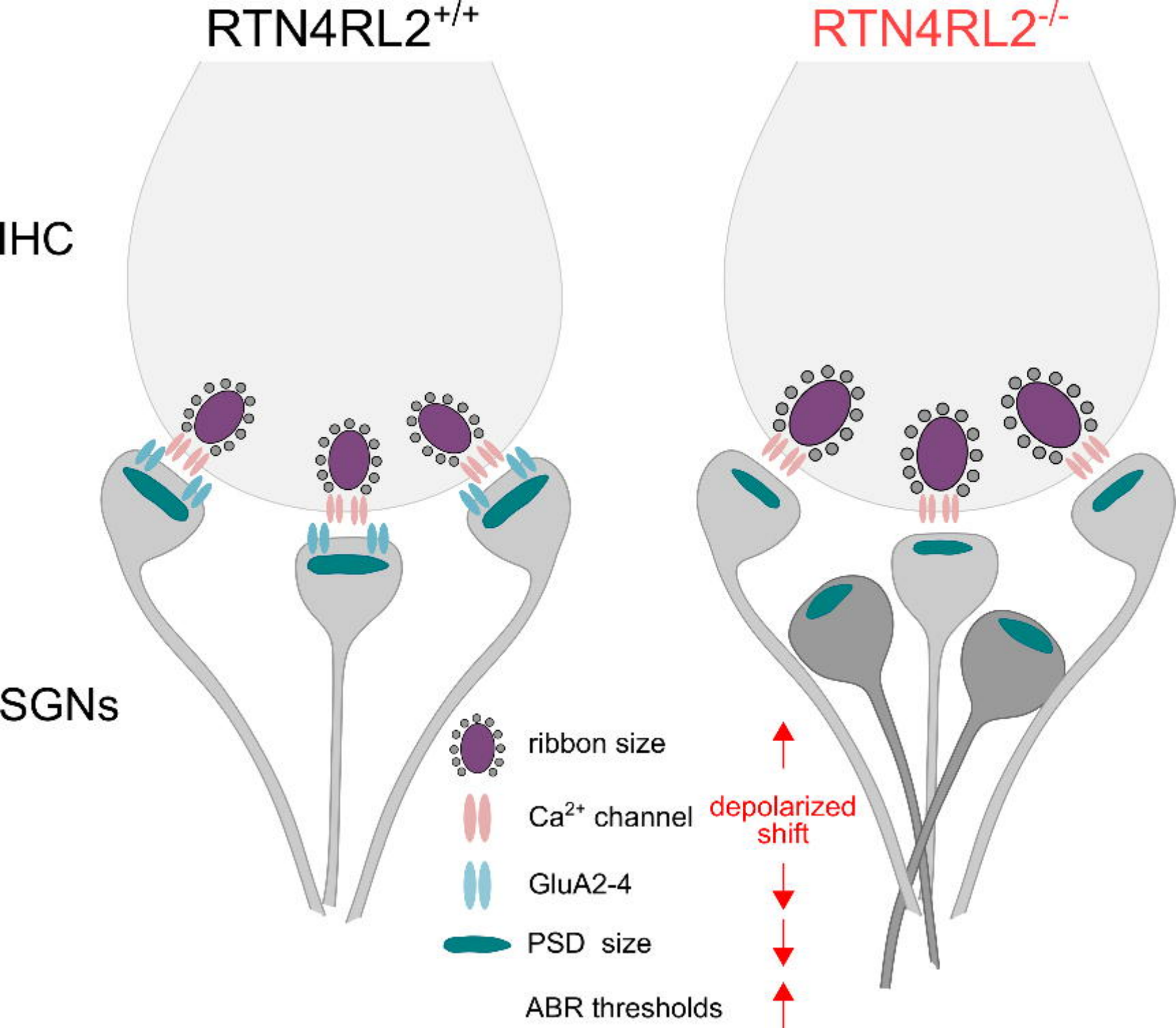
RTN4RL2+/+
RTN4RL2-/-
IHC
SGNs
ribbon size
Ca2+ channel
GluA2-4
PSD size
ABR thresholds
depolarized shift